ACS Catalysis

pubs.acs.org/acscatalysis

Research Article

Linking Bulk and Surface Structures in Complex Mixed Oxides

Liudmyla Masliuk,[▽] Kyeonghyeon Nam,[▽] Maxwell W. Terban, Yonghyuk Lee, Pierre Kube, Daniel Delgado, Frank Girgsdies, Karsten Reuter, Robert Schlögl, Annette Trunschke, Christoph Scheurer, Mirijam Zobel, and Thomas Lunkenbein*

Cite This: *ACS Catal.* 2024, 14, 9018−9033

Read Online

ACCESS | Metrics & More | Article Recommendations | Supporting Information

ABSTRACT: The interface between a solid catalyst and the reacting medium plays a crucial role in the function of the material in catalysis. In the present work, we show that the surface termination of isostructural molybdenum−vanadium oxides is strongly linked to the real structure of the bulk. This conclusion is based on comparing (scanning) transmission electron microscopy images with pair distribution function (PDF) data obtained for $(Mo,V)O_x$ and $(Mo,V,Te,Nb)O_x$. Distance-dependent analyses of the PDF results demonstrate that $(Mo,V,Te,Nb)O_x$ exhibits stronger deviations from the averaged orthorhombic crystal structure than $(Mo,V)O_x$ in the short and intermediate regimes. These deviations are explained by higher structural diversity, which is facilitated by the increased chemical complexity of the quinary oxide and in particular by the presence of Nb. This structural diversity is seemingly important to form intrinsic bulk-like surface terminations that are highly selective in alkane oxidation. More rigid $(Mo,V)O_x$ is characterized by defective surfaces that are more active but less selective for the same reactions. In line with machine learning interatomic potential (MLIP) calculations, we highlight that the surface termination of $(Mo,V,Te,Nb)O_x$ is characterized by a reconfiguration of the pentagonal building blocks, causing a preferential exposure of Nb sites. The presented results foster hypotheses that chemical complexity is superior for the performance of multifunctional catalysts. The underlying principle is not the presence of multiple chemically different surface centers but instead the ability of structural diversity to optimally align and distribute the elements at the surface and, thus, to shape the structural environment around the active sites. This study experimentally evidences the origin of the structure-directing impact of the real structure of the bulk on functional interfaces and encourages the development of efficient surface engineering strategies toward improved high-performance selective oxidation catalysts.

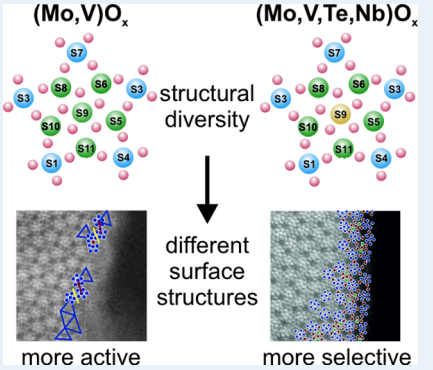

KEYWORDS: *selective oxidation, chemical electron microscopy, pair distribution function analysis, heterogeneous catalysis, acrylic acid, ethylene, structural diversity*

INTRODUCTION

The production of olefins and functionalized hydrocarbons on the surface of heterogeneous catalysts is one of the key reactions in the chemical industry to efficiently produce reactive building blocks for the consecutive synthesis of daily life products. In order to maintain the sustainability chain from natural gases and crude oil, there is a strong desire to enhance their production efficiencies.[1] With the discovery of polycrystalline MoV oxides,[2] potential catalyst systems have been identified that are highly suited for introducing functionality into short-chain alkanes.[2−4] These materials are structurally extremely complex, and the question arises as to whether this complexity is decisive for their function.

Within this family of structurally related materials, catalyst performance depends sensitively on the composition, synthesis, and pretreatment of the precursor.[5−9] Novel synthetic protocols have especially been developed to optimize the catalytic efficiency by tailoring the microstructure.[10,11] MoV-based mixed oxides that crystallize in an orthorhombic phase, referred to as M1-type,[7,9,12−15] show particularly great potential in the oxidative dehydrogenation of ethane (ODE) as well as (amm)oxidation of propane to acrylonitrile and acrylic acid, respectively. The high yield of these oxides with respect to the desired selective oxidation product has been explained by the concept of "seven pillars", which includes the importance of structural effects, such as site isolation, host structure, and multifunctionality, as descriptors for catalytic performance.[16]

Thus, understanding the structures of these complex oxides is crucial. For these oxides, scanning transmission electron microscopy (STEM) has been, for instance, used to investigate

Received: November 1, 2023
Revised: May 7, 2024
Accepted: May 8, 2024
Published: May 29, 2024

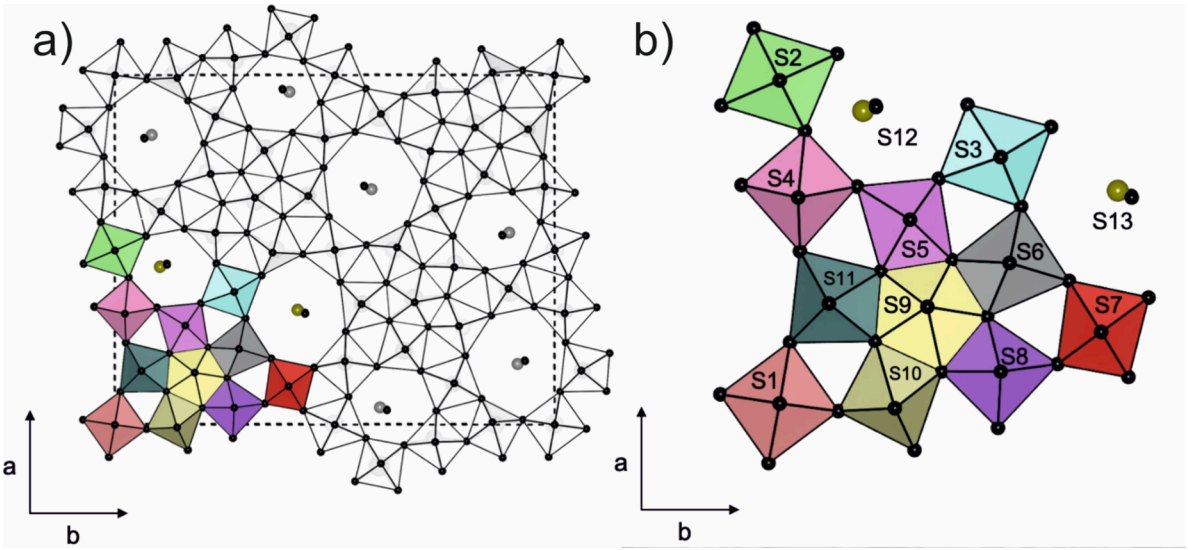

Figure 1. The structures of $(Mo,V)O_x$and $(Mo,V,Te,Nb)O_x$. (a and b) Structural models of orthorhombic mixed molybdenum and vanadium oxides; the unit cell of $(Mo,V,Te,Nb)O_x$ (ICSD 55097) viewed along the crystallographic *c*-axis was used for illustration purposes. The labeling of the metal sites coordinated by oxygen atoms octahedrally or pentagonal-bipyramidally as well as the metal sites in the channels is given in (b).

their nanostructures.[10,17−23] These studies either focus on a detailed description of the intrinsic local structure or follow the structural evolution *in situ* by environmental transmission electron microscopy (ETEM) analysis.[24,25] Besides the visualization of defects,[17,19,23,26] structural disorder,[18,22] and mixed metal site occupation,[27] high-resolution STEM measurements have focused on a detailed and atomistic description of the surface structure and suggested that {120} and {210} surface terminations for $(Mo,V,Te,Nb)O_x$ are most selective in the oxidative conversion of small alkanes.[28] Furthermore, reaction-induced local structural modifications at the atomic scale have been visualized for orthorhombic $(Mo,V,Te)O_x$ and $(Mo,V,Te,Nb)O_x$ using ETEM. These studies have demonstrated a depletion of Te moieties from the structural channels.[24,25] This depletion was not observed in *ex situ* investigations of phase-pure $(Mo,V,Te,Nb)O_x$.[29] A migration of Te species to the surface was also found by *in situ* X-ray photoelectron spectroscopy (XPS) measurements. Accordingly, surface enrichment with Te species is necessary to obtain high selectivity by breaking up extended vanadium oxide sites, implying the *in situ* genesis of site isolation.[30] The reversibility of the gas-phase-induced surface changes depends on the chemical composition of the M1 phase.[30] In general, a dynamic and reversible response to the applied chemical potential is associated with high selectivity in alkane oxidation.

Complementary studies using X-ray diffraction (XRD) experiments reveal the responses of the crystallographic average structure to the reaction media, *e.g.*, size changes of structural channels or phase transformations.[6,7,31,32] Although these studies do not provide direct information on the details of local structuring, comparative analysis of diffraction data before and after catalysis can yield insights into short-range phenomena, such as defects or lattice strain transmitted to the surface.[33] Further information on the average short-range order can be obtained directly by pair distribution function (PDF) analysis. A recent example highlights that combined extended X-ray absorption fine structure (EXAFS) and PDF analysis enable structural insights during the crystallization of $(Mo,V,Te,Nb)O_x$, which was prepared by the slurry method.[34] In this study, it was found that pentagonal building blocks started to form at calcination temperatures above 350 °C.

In selective oxidation catalysts, the bulk structure often acts as a support for the formation of an intrinsically decoupled surface that subsequently transforms into the active phase under operation conditions.[35,36] For instance, it has been shown that postsynthetic catalyst tailoring by epitaxial grown M1-type building blocks on the surface of a nonselective oxide significantly increases the selectivity in the ammoxidation of propane.[37] This finding implies that as long as M1-type building blocks are present at the surface, the catalytic performances of various M1-type catalysts should be similar. However, in reality the catalytic behaviors of isostructural oxides can be vastly different. This would suggest that different surface structures can exist that are responsible for the different catalytic performances. Furthermore, this indicates that the surface structures are not solely related to a thermal equilibrium with the gas phase but that anchoring to the real structures of the bulk also exists.

Here, we untangle this structural anchor by combining the results obtained from STEM imaging, calculations obtained from machine learning interatomic potential (MLIP), and the quantitative analysis of PDF data using isostructural $(Mo,V)O_x$ and $(Mo,V,Te,Nb)O_x$ as an example. We will show that the degree of structural diversity in the bulk is responsible for adjusting the final surface structure after calcination; as such, the study extends Grasselli's idea of the ideal crystal structure as a descriptor for the surface structures.[38]

RESULTS

The Ideal Structures of $(Mo,V)O_x$ and $(Mo,V,Te,Nb)O_x$.

Phase-pure $(Mo,V)O_x$ (Figure S1a) and $(Mo,V,Te,Nb)O_x$ (Figure S1b) have been synthesized via the hydrothermal route. The samples are investigated in their pristine states after thermal treatment in an Ar atmosphere. Identical aliquots of the same sample batches have been investigated elsewhere, which also includes a detailed discussion of their real structures and (local) composition.[22,23,39] The lattice parameters of $(Mo,V)O_x$ (a = 21.0964(4) Å, b = 26.5349(3) Å, c =

https://doi.org/10.1021/acscatal.3c05230
ACS Catal. 2024, 14, 9018−9033

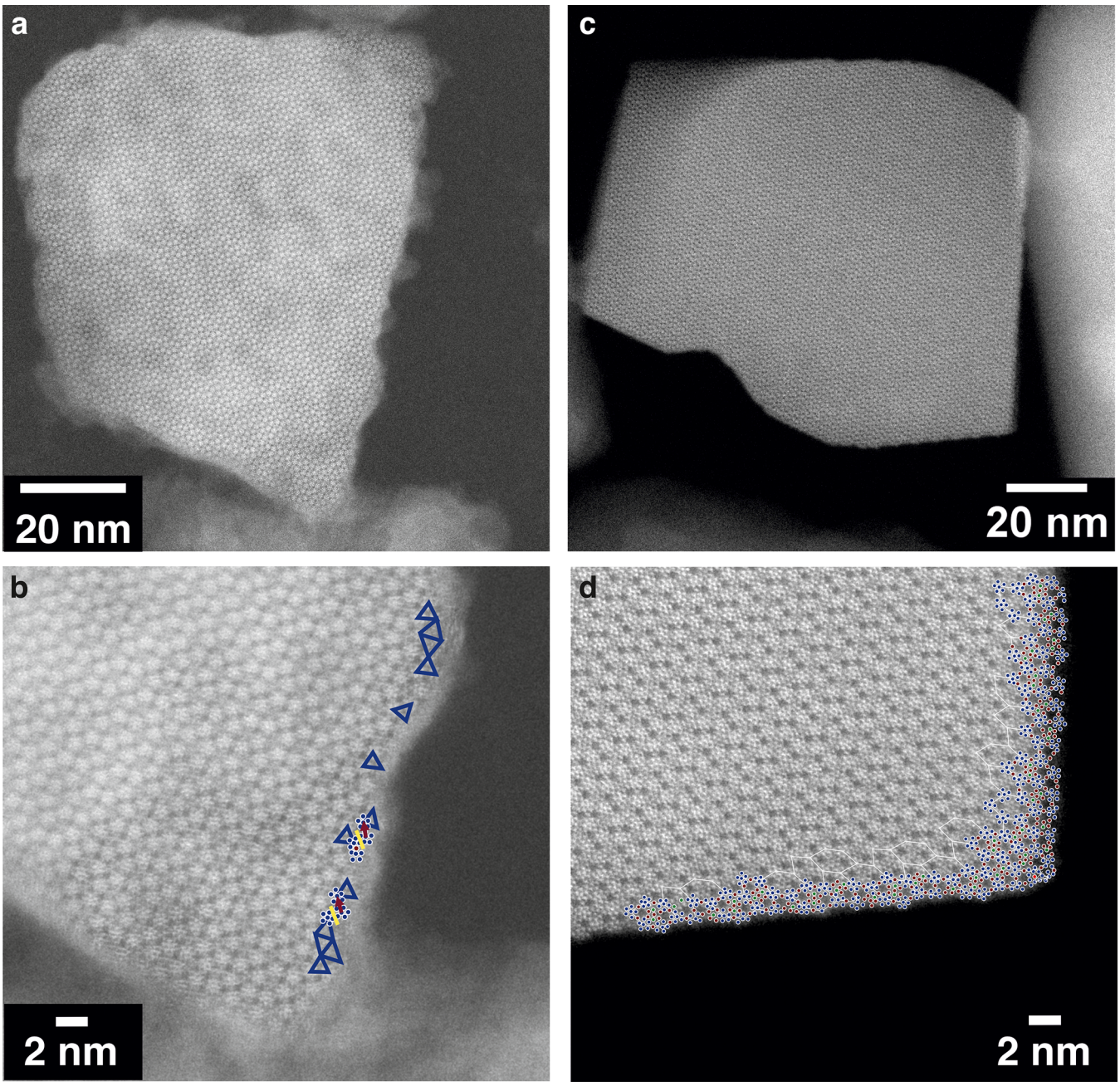

Figure 2. The real surface structures of $(Mo,V)O_x$and $(Mo,V,Te,Nb)O_x$. (a and b) Annular dark-field (ADF)-STEM images of the surface regions of $(Mo,V)O_x$. The colored surface motifs highlight the different surface structures: blue triangles represent the triangular structures, red arrows express translated motifs, yellow bars indicate mirrored motifs, and a red circle displays a shared motif. (c and d) ADF-STEM images of the surface regions of $(Mo,V,Te,Nb)O_x$. Blue circles indicate pentagonal building blocks, red circles represent mixed V/Mo-containing sites, and green circles highlight channel sites. The original images and the corresponding fast Fourier transform (FFT) analysis are presented in Figures S5−S7.

4.00001(6) Å, V = 2239.17(6) Å^3) are noticeably smaller than those for $(Mo,V,Te,Nb)O_x$ (a = 21.2138(7) Å, b = 26.6895(10) Å, c = 4.01367(12) Å, V = 2272.48(13) Å^3).

These complex and compositionally flexible oxides are based on molybdenum and vanadium and crystallize in the same orthorhombic structure (Figure 1a, space group *Pba*2). The metal atoms are octahedrally or pentagonal bipyramidally coordinated by oxygen atoms. The interconnection of the polyhedra via corners and edges as well as the local fivefold symmetry leads to the creation of an open structure with stabilizing pillars, which are formed by pentagonal units, and two different types of channels along the crystallographic *c*-direction. In the channels, further metal positions, such as V or Te are located (Figure 1a). The nomenclature of the different metal positions is given in Figure 1b. The main differences can be found in the occupancies of the structural channels and the center of the pentagonal building blocks.

For $(Mo,V)O_x$, the hexagonal channel sites are partially occupied with V. The occupancy depends on the synthesis and consequently different values between 4% and 49% have been reported.[7,40] For $(Mo,V,Te,Nb)O_x$, the hexagonal channels are partially filled with Te (occupancy of 69% or 74%).[14,41] In addition, the Te cations are off-centered and can be shifted toward the S2 metal site. This shift toward the S2 site of the Te

https://doi.org/10.1021/acscatal.3c05230
ACS Catal. 2024, 14, 9018−9033

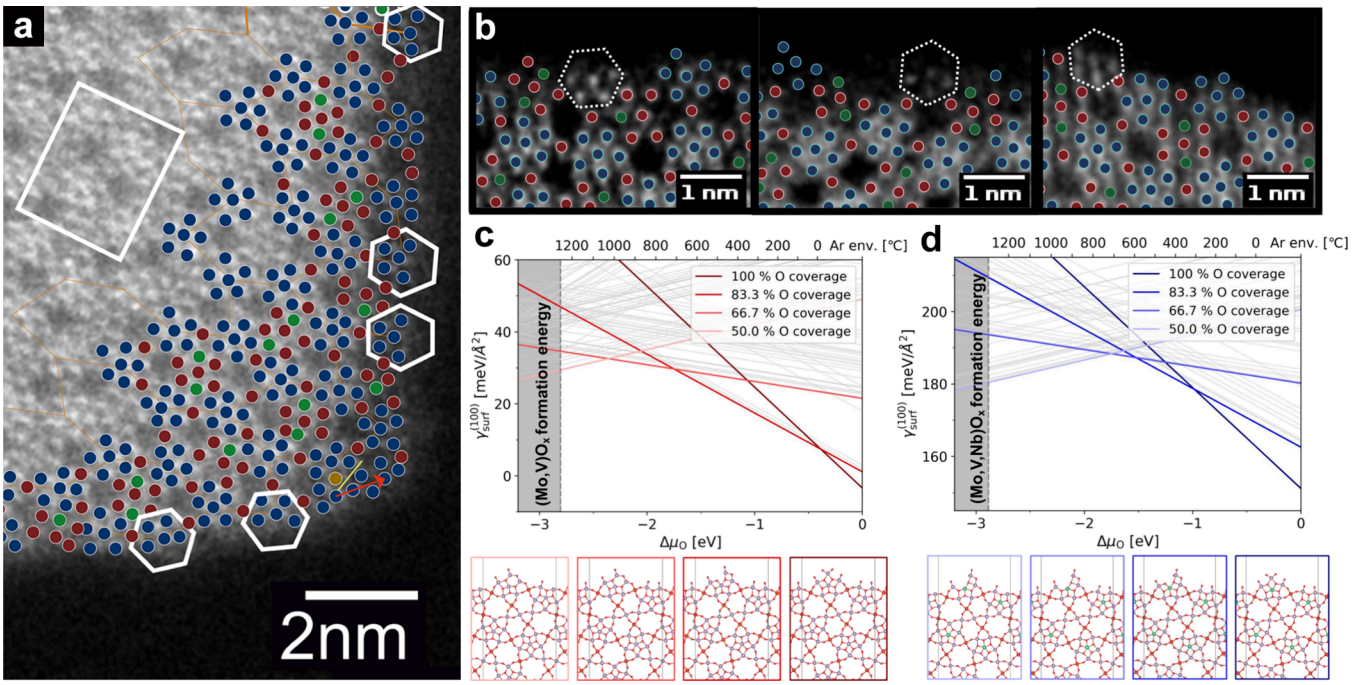

Figure 3. The exposure of Nb sites on the surface of M1 catalysts. (a and b) ADF-STEM images of the (Mo,V,Te,Nb)O_x surface regions at different locations. The original images of (b) are presented in the Supporting Information (Figure S8). The white rectangle in (a) indicates the unit cell. Blue circles indicate pentagonal building blocks, red circles represent mixed V/Mo containing sites, and green circles highlight channel sites. White hexagons denote pentagonal building blocks with a missing metal site. (c and d) Phase diagrams of various surface terminations on a (100) facet of (Mo,V)O_x and (Mo,V,Nb)O_x, respectively. The most stable (100) surface structures corresponding to the lowest lines as a function of the oxygen chemical potential are displayed below each phase diagram.

moieties ultimately induces a local cation displacement at the S2 sites.[22,42] A displacement of the S2 site in isostructural (Mo,V)O_x has not yet been observed by STEM imaging. However, its presence was suggested by single crystal analysis.[40]

These oxides can be further distinguished by the composition of the center of the pentagonal {(M)Mo_5} (M= Mo or Nb) building blocks (S9 metal site). While this building block is entirely composed of Mo^{6+} cations in (Mo,V)O_x, in (Mo,V,Te,Nb)O_x the centers of the pentagonal building blocks are composed of pentagonal NbO_7 bipyramids.[7,13,27,40,43] The presence of Nb and Te in the quinary oxide has been confirmed by energy dispersive X-ray spectroscopy (EDX) measurements (Figure S2) and elemental analysis.

The Real Structures of (Mo,V)O_x and (Mo,V,Te,Nb)O_x. It is known that (Mo,V)O_x and (Mo,V,Te,Nb)O_x exhibit vastly different activity and selectivity contributions in the selective oxidation of light alkanes to functionalized hydrocarbons (see also Figure S3).[40,44] In general, (Mo,V,Te,Nb)O_x is more selective, while (Mo,V)O_x is more active. In a first attempt, we seek to identify the origin of the different catalytic behaviors in variations of the real structures of the surfaces of these isostructural oxides.

The Real Structure of the Surface. Figure 2 shows high-resolution STEM (HR-STEM) micrographs of thermally equilibrated pristine (Mo,V)O_x (Figure 2a and b) and (Mo,V,Te,Nb)O_x particles (Figure 2c and d). Different surface terminations are observed that could explain the difference in the catalytic performance. Similar to previous reports,[28] the surface of (Mo,V)O_x (Figure 2a) is composed of rough and defective nanofacets that can be embedded by blurred regions, while the surface of (Mo,V,Te,Nb)O_x (Figure 2c) appears much smoother and is closely related to the bulk structure. This observation is in line with a previous study.[28]

Due to the observed surface roughness and the presence of surface defects, a clear assignment of the crystallographic surface terminations is unfeasible for (Mo,V)O_x. This is consistent with a previous HR-STEM investigation in which a total of 1900 local motifs and 22 intergrown and extended defects were detected within 31 (Mo,V)O_x particles (Figure S4).[23] Similar to this study, a large fraction of the local motifs appeared close to the surface (Figure 2b). Assuming that the average metal site occupancy as determined by X-ray diffraction extents to the surface, *i.e.*, applying the idea introduced by Grasselli,[38] and applying this information to the exposed metal sites at the surface obtained from STEM imaging, the surface composition of one crystal was approximated to be ($MoV_{0.38}M_{0.11}$)O_x (M = Mo and/or V).[23] For further details, we refer to the Methods. The uncertainty arises from the presence of disordered surface layers. Recent electron energy loss spectroscopy analysis has shown that the lateral surface of (Mo,V)O_x is Mo enriched, while the apical surfaces exhibit more V.[39] Under the assumption that M = Mo, this would suggest a single-particle surface composition of ($MoV_{0.34}$)O_x, which would represent a higher V content compared to the average surface composition of ($MoV_{0.23}$)O_x as determined by XPS. However, it is still lower than the bulk composition of ($MoV_{0.42}$)O_x, which was obtained by X-ray fluorescence (XRF) measurements, suggesting a Mo-rich surface layer.[39]

The ADF-STEM image of (Mo,V,Te,Nb)O_x suggests that amorphous surface layers of different composition surrounding particles of the quinary oxide are absent, which is in line with a previous study.[28] In addition, surface defects only occur where

https://doi.org/10.1021/acscatal.3c05230
ACS Catal. 2024, 14, 9018−9033

the surface facets change (Figure 3a). In the same way as described for $(Mo,V)O_x$, a surface composition was approximated for the fraction of the $(Mo,V,Te,Nb)O_x$ particle presented in Figure 2d (see Methods for details). This way, the local surface composition was found to be $(MoV_{0.16}Te_{0.00}Nb_{0.08})O_x$, indicating a depletion of the Te and V contents from the bulk composition $(MoV_{0.20}Te_{0.08}Nb_{0.23})O_x$, which was determined from XRF analysis. The Nb and Te contents at the surface are seemingly strongly affected by this local approximation, suggesting that in this particle Te and Nb are depleted from the surface. Further examples in Figure 3b, however, suggest that channel sites are exposed to the environment. In $(Mo,V,Te,Nb)O_x$, these channel sites are occupied by Te (Figure 1). These examples highlight that the surface composition is altered locally and that the exact surface composition is particle-dependent. Figures 3a and b further indicate that the surfaces of $(Mo,V,Te,Nb)O_x$ are terminated by pentagonal building blocks and half-piped open channels that guarantee surface access of mixed molybdenum and vanadium sites. These surface terminations have been discussed previously.[30,45] In addition, the same image illustrates that at the surface some molybdenum containing edge-sharing octahedra of the pentagonal building blocks are missing. This implies a partial exposure of the central Nb sites (Figures 3a and b, white hexagons, Figure S9) to the environment.

MLIP Surface Simulations. To understand the appearance of the surface found by STEM imaging (Figures 2 and 3a and b) in greater detail and to shed light on the underlying energetic driving forces at the atomistic level, surface simulations via MLIP trained on density functional theory (DFT) level calculations have been performed. Conventional slab calculations conducted by DFT are impractical to study the surface structure, energetics, and reconstructions due to the large primitive cell of the M1 family, which hosts a minimum of, without occupational disorder, 152 atoms. The modeling is thus based on MLIP trained with DFT calculations of earlier experimental studies, which have revealed that M1 crystals are composed of stacked layers connected by metal−oxygen bonds along the ⟨001⟩ direction to form rod-like structures.[13,40,45] The mesoscopic crystals then predominantly grow in shapes with basal (001) surface termination and (hk0) prismatic side faces.[13,46] To investigate the (001) surfaces, the M1 crystallites have been decomposed accordingly into tractable rod-like local structures, akin to those that were experimentally observed and tabulated in a previous study.[23] As these local structures cannot completely mimic the surface of the M1 catalysts, staged training protocols for MLIP[47] from local motifs to surfaces constructed from (1 × 1) cells were employed to link the local motifs and bulk structures. This way, understanding of the local surface reconstructions can be provided.

In detail, the simplest motif (termed "pillar" in the following) consists of one pentagonal motif with six metal atoms that are stacked in the (001) direction (crystallographic *c*-direction, *z*-axis in the calculation).[23] To explore the effect of the heat treatment on the relative stability of these motifs and how these structures are related to real experimental conditions in alkane oxidation, we have simulated each surface motif with varying oxygen contents. The resulting configurations have been calculated independently for each of the investigated motif structures. Starting from the fully oxidized motifs of $(Mo,V,Nb)O_x$ taken from the bulk structure, oxygen atoms have been removed stepwise until a motif with the 50% coverage of the possible oxygen occupation sites has been reached. The same procedure has been applied for the corresponding series of $(Mo,V)O_x$ motifs, derived from the bulk structures of Mo_5O_{14} and $(Mo,V)O_x$. Then, each MLIP trained on motif structures has been further trained on the (1 × 1) surface taken from $(Mo,V,Nb)O_x$ and ternary M1 $(Mo,V)O_x$ bulk materials, respectively. To avoid the high memory requirement of five -element GAP in a complexed system and to untangle and simplify the effect of Nb-centered pentagonal motif from Te partial occupation, Te atoms have not taken into account for the simulations. To judge which of the resulting surfaces is most likely observed in experiments, we then make use of *ab initio* thermodynamics[48] and calculate the surface free energy change $\Delta\gamma_{surf}^{(100)}$ in equilibrium with an oxygen environment at a prescribed chemical potential. The details of the calculation are given in the Methods and Supporting Information (Figures S10−S15 and Tables S1−S2).

The relative stabilities of the most stable, fully optimized surface terminations on the (100) facet with varying oxygen contents are shown in the phase diagrams for $(Mo,V)O_x$ (Figure 3c) and $(Mo,V,Nb)O_x$ (Figure 3d) surfaces, respectively. The lowest surface free energy ($\Delta\gamma$) line yields the predominant surface termination under the given conditions, and a phase transition is expected to occur at the intersection of these lines. In detail, in the case of $(Mo,V)O_x$, the (100) surface with 83.3% O coverage is stabilized at low oxygen chemical potentials ($\Delta\mu_O < -0.4$ eV) and transforms into the lowest energy surface when $\Delta\mu_O$ is larger than −0.4 eV. Similarly, for $(Mo,V,Nb)O_x$, the surface with 83.3% O coverage is the most stable at $\Delta\mu_O < -1$ eV, while the surface with 100% O coverage is stabilized when $\Delta\mu_O$ is higher than −1 eV. In the case of $(Mo,V)O_x$ (Figure 3c), the pentagonal-shaped pillars typically rearrange into a quasi-rectangular shape. Such a rearrangement is due to the relatively flexible Mo−O local coordination environments, resulting from shallow minima in a rather soft potential energy landscape (Figure 3c). This finding is experimentally supported by the occurrence of an amorphous rim surrounding the $(Mo,V)O_x$ particles (Figure 2a and b) indicating that different conformers can coexist at the surface. This is not expected to occur in the regular bulk due to the heightened energy barriers imposed by the enclosing, regular bonding structures but may be plausible at grain boundaries or surfaces. In the case of $(Mo,V,Nb)O_x$, more hexagonal Mo−O polygons, each enclosing a Nb−O polyhedron, emerge as low-energy motifs. Their overall rearrangement is rather moderate compared to those of the Mo-centered motif and might be driven by the local Nb−O hybridization.

The local potential energy landscape that determines the Nb−O coordination environment seems to be dominated by few and rather deep local minima and dominates the surrounding Mo−O polyhedra, thus enforcing a restructuring of the latter. The resulting arrangements of the heavy atoms that are visible in the STEM images exhibit partially angles that are larger than 108° (Figure 3a, b white hexagons). Thus, they should be interpreted as early stages toward a hexagonal arrangement that forms around the central Nb with missing Mo-corners (see white hexagons in Figure 3b) rather than a pentagonal Mo ring around the Nb, which is the dominant bulk motif. The phase transition temperature (as computed from $\Delta\mu_O$ for the given atmosphere) of $(Mo,V,Nb)O_x$ (100) surfaces is around 300 °C higher than that of $(Mo,V)O_x$ (100)

https://doi.org/10.1021/acscatal.3c05230
ACS Catal. 2024, 14, 9018−9033

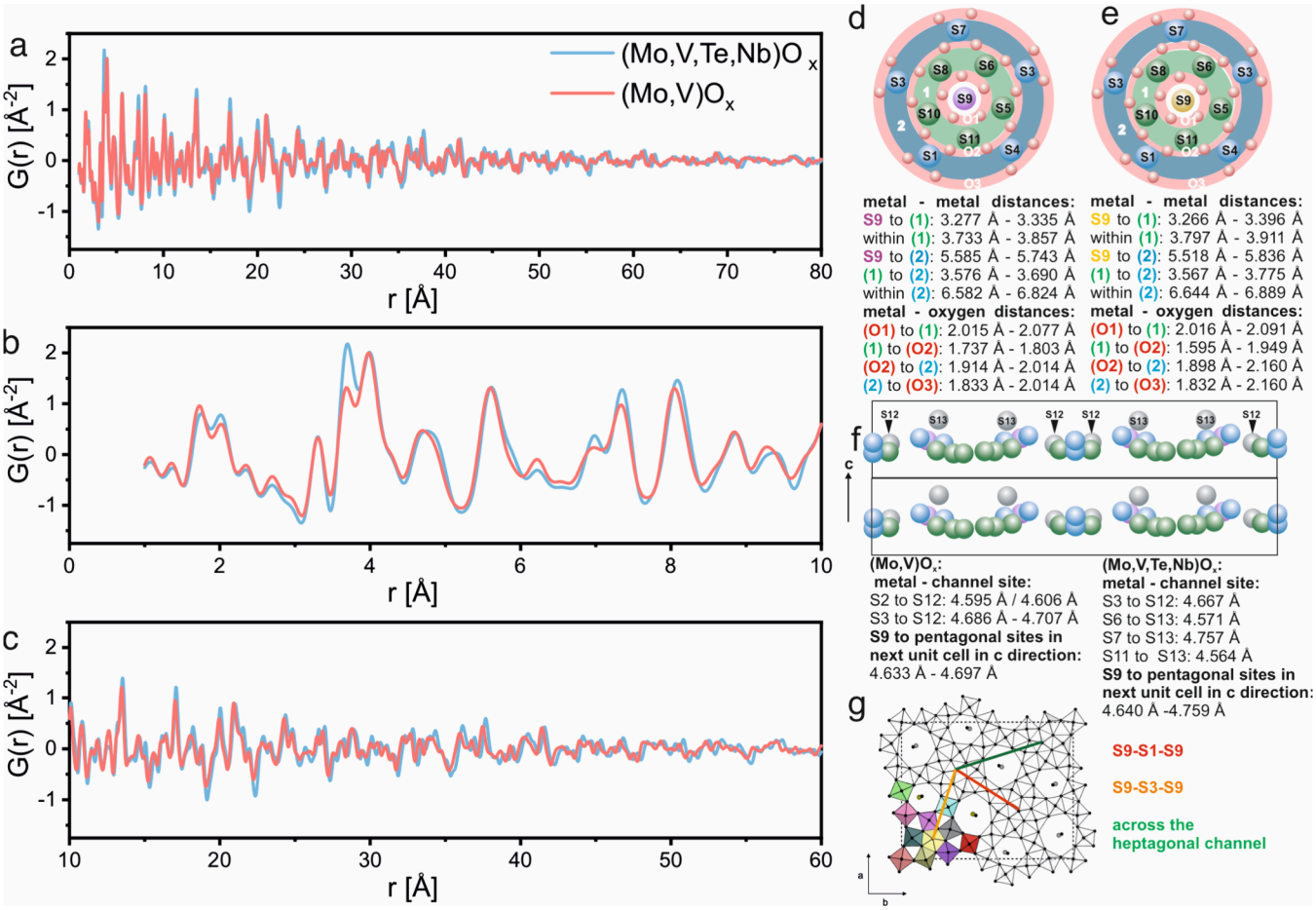

Figure 4. Experimental PDFs of $(Mo,V)O_x$ (red) and $(Mo,V,Te,Nb)O_x$ (blue) for different ranges: (a) 1−80 Å, (b) 1−10 Å, and (c) 10−60 Å. (d−g) Distances in $(Mo,V)O_x$ and $(Mo,V,Te,Nb)O_x$. (d) Metal−metal distances and (e) metal−oxygen distances in $(Mo,V)O_x$ (d) and $(Mo,V,Te,Nb)O_x$ (e) as derived from averaged crystal structural models.[13,40] Distances refer to the coordination environments occupied by metals and oxygen and are numbered consecutively with respect to the central metal sites of the pentagonal building blocks. The coordination spheres are highlighted by colored annular areas. Green spheres denote Mo metal sites of the pentagonal building block, blue spheres correspond to metal sites in corner sharing octahedra, the orange sphere highlights Nb, and red indicates oxygen. (f) Schematic view of the crystal structure in the [010] direction. The corrugation of the metal sites along [001] is highlighted. The distances below the scheme correspond to the peak observed at around 4.7 Å, which arises from metal-to-channel site distances and metal−metal distances within neighboring unit cells stacked along the [001] direction. (g) Structural model of the orthorhombic M1 phase superimposed with different distances (colored lines). The red, orange, and green lines denote S9−S1−S9, S9−S3−S9, and S9 $(-1 + x, y, z)$−S9 $(-05 + x, 0.5 + y, z)$ distances, respectively.

surfaces at the residual O_2 partial pressure in an Ar atmosphere. The severe rearrangement from bulk structure and the lower temperature phase transition of the $(Mo,V)O_x$ (100) surfaces explains the lower stability of its (hk0) surfaces when compared to the moderate rearrangement and the high phase transition temperature of the related $(Mo,V,Nb)O_x$ (hk0) surfaces. The rearrangement of $(Mo,V,Nb)O_x$ to the open hexagonal structure also results in more easily periodically replicated edge structures, which may rationalize the differences in the surface reconstruction behavior of $(Mo,V,Te,Nb)O_x$ and $(Mo,V)O_x$. The stable open hexagonal structure of the $(Mo,V,Nb)O_x$ can be easily incorporated in the smooth surface of $(Mo,V,Te,Nb)O_x$ compared to the rough and defective surface of $(Mo,V)O_x$ via stabilization of the exposed central Nb sites along with the half-piped open channels.

In summary, bulk and surface structures as well as composition are not synonymous in M1-type catalysts. The surface structure is closely related to not only the chemical potential of the gas phase but also to the chemical potential of the underlying bulk. Thus, the observed differences in the thermally equilibrated surface structures between $(Mo,V,Te,Nb)O_x$ and $(Mo,V)O_x$ suggest that a bulk property must exist that is linked to the different appearances of the surface structures. Next, we seek to qualitatively and quantitatively identify and describe this bulk property.

Analysis of the Short-Range Order by Pair Distribution Function (PDF) Analysis. STEM examples of the local bulk structures are presented in Figures S16−S20, demonstrating that the bulk real structures of $(Mo,V,Te,Nb)O_x$ and $(Mo,V)O_x$ differ. Overall, $(Mo,V,Te,Nb)O_x$ is less defective than $(Mo,V)O_x$.[23] Altogether, the STEM analyses of the bulk imply that the chemical complexity affects the short-range order of these oxides. In order to explore how short-range order in the bulk and surface structures can be linked, a PDF study has been conducted.

PDF Analysis. PDF analysis is a powerful technique to characterize the short-range order in disordered materials.[49] This also includes crystalline materials that exhibit intrinsic nanostructures or chemical short-range order, as is the case for

https://doi.org/10.1021/acscatal.3c05230
ACS Catal. 2024, 14, 9018−9033

$(Mo,V)O_x$ and $(Mo,V,Te,Nb)O_x$.[19,38,43,50,51] Here, the PDF is obtained by Fourier transformation of high-energy X-ray scattering data measured over a large range of momentum transfer (Figure S21). The PDF corresponds to a weighted histogram of interatomic distances in real space, and the technique has recently been applied to characterize short-range order in heterogeneous catalysts and metal oxides.[52−54]

The experimental PDFs of $(Mo,V)O_x$ and $(Mo,V,Te,Nb)O_x$ up to 80 Å are shown in Figure 4a−c. Schematic drawings that highlight individual metal−metal and metal−oxygen distances of the pentagonal building blocks and the stacking along the crystallographic *c*-axis for $(Mo,V)O_x$ and $(Mo,V,Te,Nb)O_x$ are presented in Figure 4d−f. Further details on the distribution of distances are presented in the Supporting Information (Figures S22−S23). Notably, the peaks in the short-range regime <10 Å appear at similar positions with differences primarily in the relative intensities at 1.72 and 2.06 Å, as well as at 3.69 and 3.96 Å (Figure 4b). The former doublet corresponds to metal−oxygen distances, while the latter stems from the metal−metal distances (Figures 4d and e) within the first coordination sphere of the pentagonal building blocks. Given the corrugated stacking of the metal cations and channel sites (S12 and S13) along the crystallographic *c*-axis (Figure 4f), the peak centered around 4.70 Å can denote distances from S2, S3, S6, S7, or S11 to S12 and S13 centers and from S9 to S5, S6, S8, S10, or S11 centers of the vicinal unit cell stacked along the [001] direction. The maxima at 5.60 Å can be assigned to distances from the S9 site of the pentagonal building block to the metal sites within coordination sphere 2 (Figures 4d and e).

For $(Mo,V)O_x$, the peak intensity that corresponds to a distance of 1.72 Å is enhanced compared to the peak at 2.06 Å. Both intensities are almost equal for $(Mo,V,Te,Nb)O_x$. The metal−oxygen bonds of the pentagonal building blocks (Figures 4d and e), corner sharing octahedra, and channel sites (Figure S22) would, however, suggest an almost equal distribution of the metal−oxygen bond lengths for both oxides as was found for $(Mo,V,Te,Nb)O_x$. For $(Mo,V)O_x$, two significant deviations occurred that could be assigned to the structure around the S2 sites, which have been discussed as potential active sites,[25,38] and the occupancies of the hexagonal channels of $(Mo,V)O_x$. An integral splitting of the S2 site has been described previously by single crystal X-ray diffraction analysis.[40] This splitting leads to a separation of metal−oxygen bond distances (2.06, 2.12, 1.74, and 1.76 Å) in the basal plane of the S2 site. In $(Mo,V,Te,Nb)O_x$, this displacement seems to occur only locally and is lost in the crystallographic averaging of the XRD measurements.[22] A similar displacement at the S2 site was observed by diffraction analysis in orthorhombic $(Mo,V,Sb)O_x$.[15] In addition, the V−O and Te−O bond lengths representing the metal sites within the hexagonal channels differ. The V−O distances within the hexagonal channels of $(Mo,V)O_x$ are 1.56 and 1.52 Å, while the Te−O distance in $(Mo,V,Te,Nb)O_x$ was found to be on average 2.24 Å.[13,40] These examples could explain the variation in the ratio of the metal−oxygen peak intensities centered around 1.73 and 2.02 Å.

The first peak of the second doublet at 3.69 and 3.96 Å corresponds to metal−metal distances of the pentagonal building blocks and their surrounding edge-sharing octahedra (Figure 4b). They are similar for both oxides (Figures 4d and e). However, for $(Mo,V)O_x$, the peak at 3.69 Å is suppressed compared to the peak at 3.96 Å and to $(Mo,V,Te,Nb)O_x$. The peak at 3.96 Å can be assigned to distances from the central site of the heptagonal channels to the vicinal metal cations (Figure S23). It was found for $(Mo,V)O_x$ that the heptagonal channel sites (oxygen or vanadium) are centered, which results in distances of around 4 Å (Figure S23). For $(Mo,V,Te,Nb)O_x$, the central Te cation within the heptagonal channel is off-centered and shifted toward the S3 sites (distance of 3.75 Å). Some of the remaining internal distances are greater than 4.5 Å (Figure S23). Thus, off-centring of the Te cations can cause the increase of the peak at around 3.7 Å. Note that Te has a larger scattering power than the other metals. Thus, the contributions coming from Te are slightly increased.

Interestingly, the differences in the lattice parameter are not noticeable in the range below 10 Å (Figure 4b). However, they become apparent for larger distances (Figure 4c). The increased lattice parameter for $(Mo,V,Te,Nb)O_x$ is also reflected in the reciprocal space by a shift of the Bragg reflections to smaller scattering angles (Figure S21). We rationalize this behavior using the distances between the S9 site as an example. As can be seen from the red line Figure 4g, the S9−S1−S9 distances of $(Mo,V)O_x$ (11.31 Å) and $(Mo,V,Te,Nb)O_x$ (11.31 Å) are the same. The structure slightly expands if distances across different corner sharing octahedra with mixed metal site occupation are measured, such as the S9−S3−S9 distances (Figure 4g, orange line; 11.22 Å for $(Mo,V,Te,Nb)O_x$ versus 11.14 Å for $(Mo,V)O_x$). The S3 site connects hexagonal with heptagonal channels and is known to exhibit fewer out-of-center distortions compared to the edge sharing metal sites of the pentagonal building block.[55] The difference in the expansion points to different degrees of distortion between these oxides. When measuring the distances across the structural channels (Figure 4g, green line), the S9−S9 distances of $(Mo,V,Te,Nb)O_x$ are also increased compared to $(Mo,V)O_x$. For S9 $(-1 + x - y, z)$−S9 $(-05 + x, 0.5 + y, z)$ the distances are, for instance, 14.04 and 14.18 Å for $(Mo,V)O_x$ and $(Mo,V,Te,Nb)O_x$, respectively. These effects are dominant for distances above 10 Å.

In addition, out-of-center displacements of the metal−oxygen polyhedra affect the real structures of the oxides significantly, which will be rationalized in the following. Out-of-center displacements in these oxides have been found to be a characteristic feature to stabilize the structure and have already been derived from an annular brightfield (ABF)-STEM analysis of $(Mo,V)O_x$.[55] The error bars that were obtained in this study can be interpreted as a descriptor for the local variation of the displacements.

We begin the discussion on the out-of-center displacements with the metal−oxygen polyhedra of the pentagonal building blocks. The metal−oxygen distances (O1−(sphere 1)−O2) of the edge sharing octahedral sites (S5, S6, S8, S10, and S11) within the pentagonal building blocks differ in both oxides (Figures 4d and e), indicating that the respective metal sites are displaced out-of-center in both oxides. Compared to $(Mo,V)O_x$ (Figure 4d), the range of distances is slightly increased for $(Mo,V,Te,Nb)O_x$ (Figure 4e). This statement is derived from a comparative assessment of the differences of distances between the metal sites in sphere 1 to oxygen atoms in sphere O1 and in sphere O2. The corresponding differences are 0.278 Å (2.015−1.737 Å) and 0.274 Å (2.077−1.803 Å) for $(Mo,V)O_x$ and 0.421 Å (2.016−1.555 Å) and 0.142 Å (2.091−1.949 Å) for $(Mo,V,Te,Nb)O_x$. The on average increased variance of distances for $(Mo,V,Te,Nb)O_x$ may be needed in order to compensate for the rigidity of the central

https://doi.org/10.1021/acscatal.3c05230
ACS Catal. 2024, 14, 9018−9033

pentagonal motif in which strong Nb−O covalent bonds dominate.

Next, the corner sharing sites are discussed. The corner sharing S3, S4, and S7 sites are characterized by mixed Mo and V occupancies. While the Mo content of these sites is on average above 60% for $(Mo,V,Te,Nb)O_x$, the same parameter is significantly lower for $(Mo,V)O_x$ (38%). We interpret this value as a proxy for the disorder probability, implying that a higher occupational and chemical flexibility exists for $(Mo,V,Te,Nb)O_x$ compared to $(Mo,V)O_x$. This interpretation is based on the fact that Mo^{6+} and V^{5+} cations exhibit different out-of-center displacements in an octahedral environment.[56] We anticipate that differences in the distortions stemming from the size of the cations can be neglected, as in the same octahedral environment Mo^{6+} (ion radius of 0.59 Å) and V^{5+} (ion radius of 0.54 Å) cations are similar in size.[57] The out-of-center displacement is in line with the observed deviations of the averaged metal−oxygen distances (Figures 4d and e) and bond angles of the S3, S4, and S7 sites.[55]

Measuring Structural Diversity and Its Impact on Structural Relaxation. From the range-dependent goodness-of-fit (R_w) values that have been obtained from the different refinement ranges of the PDF data (see Figures S24−S27 and Supporting Information for discussion), the transition from the short-range structure probed by PDF analysis to the long-range structure determined by XRD analysis has been probed. The data are shown in Figure 5a and display the R_w values as a function of the starting value of the refinement range, r_s, for $(Mo,V)O_x$ and $(Mo,V,Te,Nb)O_x$. Apparently, the R_w values of $(Mo,V,Te,Nb)O_x$ are larger than the ones for $(Mo,V)O_x$ up to an r_s value of around 70 Å, which corresponds to fit ranges of 70−80 and 70−100 Å for $(Mo,V)O_x$ and $(Mo,V,Te,Nb)O_x$, respectively. For both oxides, three distinguishable regions can be approximated.

For $(Mo,V)O_x$ (Figure 5a, red circles) a small increase in r_s up to a value of approximately 20 Å, which corresponds to a fit range of 20−80 Å, leads to rapid improvement of the R_w value. This is followed by a plateau in which the R_w values fluctuate around 20%. For r_s values above 60 Å, *i.e.*, fit range of 60−80 Å, the fitting quality decreases again. Based on this information, we qualitatively estimated the distances over which the local structure averages out and approaches the structure observed by crystallography to be within the range of 20−35 Å for $(Mo,V)O_x$ (Figure 5a, lower green bar), or approximately one unit cell.

In $(Mo,V,Te,Nb)O_x$, the behavior of the three regions is different (Figure 5a, blue circles). The R_w value decays more gradually with an increase of the r_s value up to approximately 55 Å, *i.e.*, the fit range of 55−100 Å. Between r_s = 55 and 75 Å, the R_w value appears to stabilize around a minimum value of 28% and subsequently increases again. Using the same logic for $(Mo,V,Te,Nb)O_x$, the distance over which the local structures average out is larger and extends to at least 35−75 Å (Figure 5a, upper green bar), corresponding to two or three unit cells. Even at these distances, the average structure still yields worse agreement. This suggests that within the quinary oxide a larger distribution of local structural states, *i.e.*, more diversity, is present. However, the local motifs, *i.e.*, pentagonal building blocks, in $(Mo,V,Te,Nb)O_x$, are more rigid, which strains the structure beyond a unit cell, while in $(Mo,V)O_x$ the strain already decays within a single unit cell.

Furthermore, it must be noted that here is a decreasing amount of information to be fit as r_s increases, which may affect the trends of the R_w values. In addition to the impact of the surface, since the oxides are composed of nanoparticles, this is probably the cause of the increasing R_w values for large r_s. Therefore, we suggest that the distance ranges quoted for the two oxides represent an estimate of the minimum distance required for the local structures to average out.

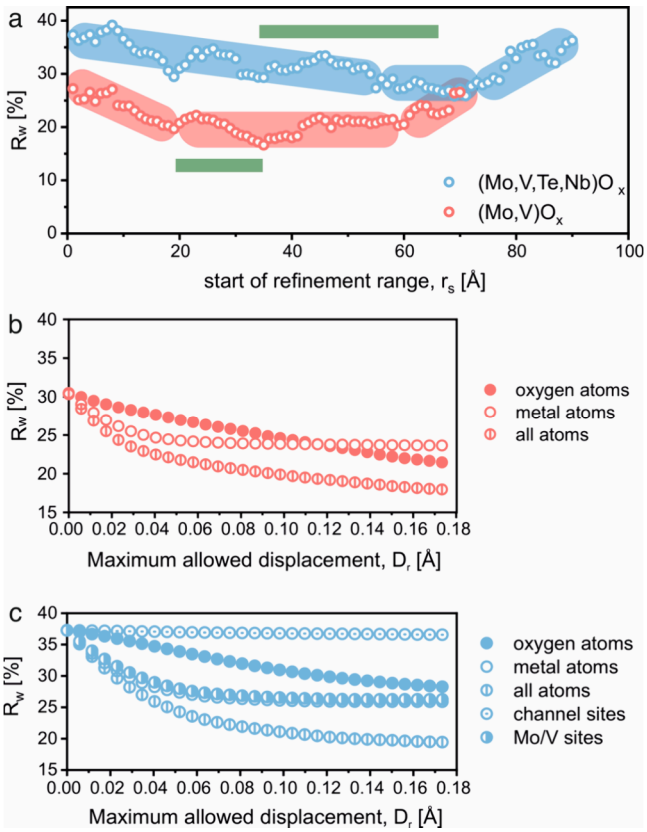

Figure 5. Trends in the goodness-of-fit (R_w) values of PDF refinements of $(Mo,V)O_x$and $(Mo,V,Te,Nb)O_x$. (a) R_w values versus the start of the refinement range. The refinement was performed up to 80 Å for $(Mo,V)O_x$ and 100 Å for $(Mo,V,Te,Nb)O_x$. This information yields an estimate for the transition from short-range to long-range structures highlighted by green bars. (b and c) Representation of R_w values as a function of the maximum of the three-dimensional (3D) displacement D_r for $(Mo,V)O_x$ and $(Mo,V,Te,Nb)O_x$, respectively, for the quantitative assessment of the out-of-center displacement.

The Magnitude of Displacive Distortion. As indicated above, different local displacements and distortions are contributing to the observed structural diversity. Next, we aimed at assessing the magnitude of displacive distortions, which is required to give a good fit to the short-range structure.

Using the rules described in the Methods, refinements over a range of 1−80 Å have been performed in which the value of the 3D displacement (D_r) has been increased stepwise. We employed this refinement method for different scenarios with both oxides as presented in Figures 5b and c. The trends of the R_w values represent how well the refinement of certain components of the structure can improve the fit of the model to the data with respect to D_r (*i.e.*, the amount of freedom allowed for the site position refinement). We tested the refinement of only oxygen site positions, only metal site positions, or all site positions for both oxides. For the quinary oxide, we also tested refining only the channel sites and only Mo/V sites. The aim was to assess for which components local

https://doi.org/10.1021/acscatal.3c05230
ACS Catal. 2024, 14, 9018−9033

distortions from the long-range structure determined by XRD are most likely and relatively how well they can describe statistics of the coordinative environment of the different atom positions in the structure (short-range structure) probed by PDF analysis.

For $(Mo,V)O_x$ (Figure 5b), the refinement of only oxygen sites results in an almost linear, but gradual, improvement in the R_w value with increasing D_r. The refinement of only the metal sites causes a more rapid improvement with shorter D_r, but the improvement quickly tapers off at larger D_r. Finally, allowing all sites to refine leads to similar agreement as with metal-only refinement at short D_r but becomes substantially better than either component alone with increasing D_r. The fit improvements in any case lend further support to the finding that short-range structural distortions are present. The real structure cannot be suitably described by localized distortions of the oxygen polyhedra around the average Mo and V sites, and the linear, gradual improvement may even suggest that the found improvement for oxygen is simply an effect of increasing model freedom. The more rapid improvement for modifications of the metal sites suggests that frustration of the metal−metal substructure is an important feature in the real structure. It is worth noting that the scattering powers of the metal atoms are much higher than those for oxygen. However, both refinements have an effect on the metal−oxygen pair distances. The best agreement for refining both components is not surprising, since there is more freedom, but it is also indicative that distortions of the metal−metal distance will also affect the polyhedra in order to maintain the correct metal−oxygen distances.

As shown in Figure 5c, $(Mo,V,Te,Nb)O_x$ exhibits some notable differences. First, modification of the channel sites alone does not account for the distortions. As with $(Mo,V)O_x$, the most important distortions occur for the metal−metal substructure. The much stronger improvement for refinement of metal sites versus oxygen sites alone in this case also suggests that local distortions from the average in the metal−metal distances are much larger than those for $(Mo,V)O_x$. This could be expected given the larger possibilities in chemical nature of the local environments. The larger distortions of the mixed occupied metal sites in corner-sharing octahedra imply that these sites, which are vicinal to the structural channels, have the largest impact on the forced, short-range structural diversity. The necessary distortions of localized metal−metal distances can be rationalized by the different out-of-center displacement of Mo and V d^0 cations in an octahedral environment. It would further imply that these local sites are high energy sites that are kinetically trapped in this open structure and are therefore thermodynamically frustrated.

We next assess possible changes in the relative coherence of certain contributions over different distance ranges. Allowing a large value of D_r for the displacement bound gives the best fits but diminishing returns in terms of physical relevance. We thus chose to optimize D_r by using the smallest value for which the most significant improvement in describing the real structure could be achieved. We therefore calculated the first and second derivatives of the curve corresponding to the "all atoms" refinements in Figure 5 for $(Mo,V)O_x$ and $(Mo,V,Te,Nb)O_x$ (Figures S28 and S29). D_r was then chosen to be the value at which the second derivative reaches approximately 0: 0.058 Å for $(Mo,V)O_x$ and 0.087 Å $(Mo,V,Te,Nb)O_x$. Note that using these values for the refinement of the experimental PDFs resulted in a significantly better description of both the short-range and long-range bulk structures of $(Mo,V,Te,Nb)O_x$ (Figure S30). For $(Mo,V)O_x$, a significantly better description of the short-range and slightly better fit for the long-range structures were observed (Figure S31).

In both cases, the local structure cannot be simply described by a relaxation of the oxygen substructure around the on-average metal sites. It is better described by slight distortions of the metal−metal substructure due to localized relaxations of discrete chemical species, which in turn is associated with some modification of the oxygen coordination. According to the analysis of the site position refinements (Figure 5), the degree of local distortions is still quite small with respect to the average structure and exhibits deviations on the order of about 0.06−0.09 Å.

Overall, the PDF analyses of $(Mo,V,Te,Nb)O_x$ and $(Mo,V)O_x$ suggest that the experimental real structures of the bulk of both compounds deviate significantly from the crystallographic average. Good agreement can be achieved when allowing displacive site distortions from the average crystallographic positions, but the magnitude of the deviations required to obtain a good fit are larger for the quinary compound. $(Mo,V)O_x$ thus seems to contain a lower degree of local structural variation in the bulk. We assume that this has to do with the lower chemical complexity of $(Mo,V)O_x$. In other words, we attribute the difference to the lower variability in the occupation of the metal atom positions in $(Mo,V)O_x$, since only Mo and V and not Mo, V, Nb, and Te are the options. As the real structure of the bulk supports the surface, different surface structures can be expected.

DISCUSSION

This study shows that the real structures of the bulk of the investigated mixed oxides are linked to the surface structure. The surface structure in turn determines the catalytic performance. Prospectively, a relation of the bulk structure to the catalytic performance via the structural diversity could be constructed for the investigated open oxides, which would allow one to judge the quality of the material in selective oxidation reactions. This is related to a common and established workflow in theoretical simulations via *ab initio* thermodynamics.

Grasselli et al. concluded that all the different elements within $(Mo,V,Te,Nb)O_x$ exhibit a specific function in the selective (am)oxidation of propane, which renders chemical complexity a highly important feature for selective alkane oxidation.[38] Furthermore, the authors already distinguished 32 possible scenarios of how the environment around the S2 site in $(Mo,V,Te,Nb)O_x$ can be composed alone, all of which had been derived from the ideal bulk structure while neglecting the real structure. Our study extents this concept and shows how the real structure of the bulk, surface structure, and catalytic performance are intimately connected. However, thermodynamic considerations due to the different thermal treatments of the two oxides should not be neglected.

Obviously, within the quinary oxide, the contribution of structural diversity is enhanced compared to the ternary oxide. The observed structural diversity is induced by the rigidity of the pentagonal building blocks, which can seemingly be adjusted by the nature of the metal occupying the central pentagonal bipyramid. Owing to their differences in oxidation state, the central metal atoms of this polyhedron, Nb^{5+} and Mo^{6+}, are both shifted toward one of the apical oxygen (O_{ap}) atoms, but to different extents (1.8169 Å for $Nb-O_{ap}$ versus

https://doi.org/10.1021/acscatal.3c05230
ACS Catal. 2024, 14, 9018−9033

1.6848 Å for Mo−O_{ap}). The shorter metal−oxygen distance indicates a higher out-of-center shift for Mo compared to Nb. This shift stresses the basal metal oxygen bonds, which is more pronounced for (Mo,V)O_x compared to (Mo,V,Te,Nb)O_x. Consequently, the strengths of the bonds are weakened and the covalent character is reduced for (Mo,V)O_x. Due to the shorter out-of-center shift, Nb exhibits a higher degree of covalency that forces the surrounding oxygen atoms to stick in their preferred positions. This is in line with the larger variance of the out-of-center displacement of the coordination sphere 1 of (Mo,V,Te,Nb)O_x compared to (Mo,V)O_x as changes in the optimal M-O bond angles can be better compensated (Figures 4d and e). This locks the structure of the pentagonal building blocks. This rigidity of the pentagonal building blocks, however, leads to problems in realizing the ideal metastable structure. To accomplish the final open structure, more flexible corner sharing Mo and V mixed occupied octrahedra are forced to arrange accordingly. This generates various substructures in the bulk with similar local minima, causing the structural diversity. Diversity in the bulk structure ultimately extends to the surface and allows for the formation of unique surface terminations.

Based on these findings, we interpret current views on the surface termination of complex mixed oxides in a more predictive sense extending the original idea, where the surface mimics the average bulk crystal structure.[58] We found that higher diversity in the local bulk structure of the oxide is linked to a more ordered surface structure. The extent of diversity in the bulk local structure may therefore act as a descriptor for the energetically accessible configuration space from which surface terminations are derived, and the atomic displacement parameter B_{eq} might act as an empirical proxy (Figure S32 and Supporting Information). Note that the present investigation utilizes ODE and the selective oxidation of propane as catalytic test reactions. The former is mechanistically a much simpler reaction compared to the selective oxidation of propane and yet the chemically more complex catalyst is more selective in both ethane and propane oxidation (Figure S3). This would support our hypothesis that chemical complexity is needed not only to avoid intrinsic surface defects but also to distribute and to align important elements at the surface. The addition of Nb enhances the selectivity toward the dehydrogenation product, as shown for the Ni−Nb−O system tested under ODE conditions, suggesting the emergence of site isolation and the reduction of electrophilic oxygen formation.[59] Figures 2 and 3 suggest that in order to obtain a bulk-like surface termination the pentagonal building block of the M1 motif needs to reconfigure, which can be best described by the removal of one metal site. As a consequence, Nb is exposed to the environment and can thus become an active site on the one hand and dilute highly active sites on the other.

Under reaction conditions, the active surface of the catalyst differs from the pristine surface structure.[60−63] The interaction of the pristine surface with the chemical potential at the interface triggers chemical dynamics, which lead to the formation of active sites. As a consequence, the resulting surface termination under working conditions determines the function of the catalyst. Which surface sites are created during this process depends on the initial surface structure and accordingly to our study on the real structure of the bulk. It is thus correspondingly important to not only understand any structural details of heterogeneous catalysts in their pristine states but also generalize this observation in order to prospectively conclude on the catalytic performance just by looking at the bulk structure.

In the present work, we have studied only one type of crystal structure. It would be interesting to investigate whether the spatial extent of local bulk structures can be a suitable (general) parameter independent of the crystal structure, which is also valid for close-packed crystal structures. Since mixed oxides of the same composition can adopt different crystal structures with various structural complexities and different sizes of unit cells, this would provide another constraining parameter in addition to the chemical composition, which can facilitate the search for more effective oxidation catalysts. In order to rationalize catalyst design strategies, key structures in oxidation catalysis have to be identified ideally from novel machine learning approaches, which have to be trained by inputting real structure information rather than from idealized structural models.

CONCLUSION

In summary we have presented a comparative and quantitative real structure analysis of (Mo,V)O_x and (Mo,V,Te,Nb)O_x that allowed for linking the real structure of the bulk with the surface structure. PDF analysis complemented by ADF-STEM imaging helped to explain the observed differences in selective oxidation reactions and attributed them to the different surface structures of the two oxides, which are a result of the intrinsic structural bulk diversity. This diversity is induced by the different central atoms of the pentagonal building blocks within the ternary and quinary oxides. As such, the term "structural diversity" is defined as the coexistence of various bulk substructures with similar local minima. PDF analysis indicates that structural diversity is more pronounced in (Mo,V,Te,Nb)O_x compared to (Mo,V)O_x as a consequence of the higher covalent character of Nb−O bonds. As such, the anisotropic displacement parameter, which can be interpreted as a quantitative measure of the structural diversity, can be postulated as a descriptor of selectivity in oxidation catalysis. In this context, PDF analysis in combination with local STEM studies represent important tools to predictively guide heterogeneous catalysis research. This methodology generates a knowledge-based quantitative relation between the real structure of the bulk (and its dynamics) and surface properties. Such a relation, when generalized to various types of materials, would be an invaluable help in modeling the behavior of hypothetically new or theoretically predicted catalysts under operation conditions. In this way, design proposals that only fulfill the requirements for static considerations can be sorted from proposals that also remain suitably reactive under performance conditions.

METHODS

Catalyst Synthesis. *(Mo,V)O_x.* Hydrothermal synthesis of the orthorhombic (Mo,V)O_x mixed oxide (internal ID 20000) was carried out in a specially built reactor (Premex Reactor AG, Lengnau, Switzerland) with a reaction vessel composed of corrosion-resistant Hastelloy C-22 (2.4602). A mixture of 9.18 g of $(NH_4)_6Mo_7O_{24}\cdot 4H_2O$ (AHM, Merck, 52 mmol Mo) dissolved in 230 g of water (Milli-Q, Merck) and 3.30 g of $VOSO_4$ (Acros Organics, 12.9 mmol V) dissolved in 30 g of water were loaded into the autoclave at room temperature. Residual air was replaced by nitrogen. Subsequently, the vessel

https://doi.org/10.1021/acscatal.3c05230
ACS Catal. 2024, 14, 9018−9033

was heated to 200 °C at a rate of 1 °C min^{-1} and held at this temperature for 17 h. The reaction mixture was stirred during the whole experiment at a rate of 100 rpm. After cooling to room temperature, a black solid was isolated by filtration (pore 5 glass frit), washed twice with distilled water, and dried at 80 °C for 16 h. To remove amorphous components in the hydrothermal product, 1 g of the powder was washed with 25 mL of oxalic acid solution (0.25 M, Acros Organics) at 60 °C for 30 min under stirring. The solid was centrifuged (5000 rpm, 30 min), washed twice with 25 mL of water, and dried at 80 °C for 16 h. Finally, a thermal treatment was performed in 100 mL min^{-1} argon flow at 400 °C (heating rate 10 °C min^{-1}) for 2 h in a rotary tube furnace (Xerion, Germany).

(Mo,V,Te,Nb)O_x. (Mo,V,Te,Nb)O_x (internal ID 23926) was synthesized by first adding a solution of 11.75 g of $(NH_4)_6Mo_7O_{24}{\cdot}4H_2O$ (56.1 mmol Mo, MERCK, lot no. A758482 622)) in 140 mL of distilled water to a solution of 3.80 g of niobium oxalate (H.C. Starck) in 30 mL of distilled water and stirring the mixture in an autoclave setup (Premex Switzerland) for 30 min. The solution was heated to 175 °C under continuous stirring (250 rpm). After 145 min at 175 °C, 30 mL of solution containing 3.86 g of $VOSO_4{\cdot}5H_2O$ (16.6 mmol V, Sigma-Aldrich, lot no. MKBX1043 V) was pumped into the autoclave at 20 mL min^{-1}. After further 145 min, 30 mL of a solution with 3.52 g of telluric acid $Te(OH)_6$ (15.3 mmol Te, Clariant, lot no. LCB 5478 D) was pumped at 20 mL min^{-1} as well. The reaction mixture was kept at 175 °C for 14 h under constant stirring and then cooled to room temperature. After the hydrothermal treatment, the resulting black-violet suspension was centrifuged and washed with distilled water thrice. The remaining solid was dried at 80 °C for 48 h in air. The black solid was activated in a rotary tube furnace (Xerion, Germany) under a constant argon flow of 100 mL min^{-1} at 650 °C for 2 h, washed with H_2O_2 to remove traces of impurities, and activated a second time in argon flow of 100 mL min^{-1} at 650 °C for 2 h.

SEM. SEM images and EDX measurements were recorded on a Hitachi S-4800 SEM equipped with a field emission gun (FEG) at acceleration voltages between 2.5 and 15 kV. Prior to imaging, the samples were dispersed on a conductive carbon tape (Plano).

XRF. The XRF measurements were performed with a PioneerS4 X-ray fluorescence spectrometer from Bruker. The measurements were conducted in vacuum using 100 mg of the sample fused together with 8.9 g of di-Li-tetraborate, resulting in a glass disc with a diameter of 40 mm. The Kα lines were analyzed by applying the calibration factors derived from the FHI-made appropriate standards.

(S)TEM Imaging. Aberration-corrected scanning transmission electron microscopy (STEM) was performed on a JEM-ARM200F microscope with CEOS CESCOR and CEOS CETCOR hexapole aberration correctors for probe and image forming lenses, respectively, along with a cold field emission gun (CFEG). The microscope was operated at 200 kV. STEM images were recorded with a JEOL annular dark-field (ADF) or bright-field (BF) detector. Prior to the measurements, the powdered material was drop deposited on a silica oxide-coated gold TEM grid. Prior to the ADF-STEM analysis, some particles were oriented along the crystallographic *c*-axis. Beam damage studies of identical samples are presented elsewhere.[22,23] The semiconvergence angle α was set to 22 mrad. ADF-STEM images were recorded with a maximum dose rate of 6200 e $Å^{-2}$ s^{-1} using an acquisition time below 40 μs per pixel. The corresponding inner and outer collection semiangles of the ADF-detectors were set from 67 to 250 mrad.

The local surface composition has been approximated as follows: (1) From the STEM images, the exposed metal site has been analyzed based on the structural model. (2) This metal site has a characteristic metal site occupancy. (3) This ratio has been summed up for all the observed surface metal sites. (4) Finally, the obtained sum formula has been normalized by the Mo content.

EFTEM Mapping. EFTEM data were collected with Gatan Imaging Filter (Quantum) CCD camera with the application of an entrance slit of 10 eV width for zero-loss collection. Thickness maps were obtained from the ratio of unfiltered and zero-loss maps and further color enhanced for clarity.

Oxidative Dehydrogenation of Ethane (ODE). The catalytic tests were carried out using a catalytic fixed-bed reactor as described elsewhere.[64] The reaction gas mixture was ($C_2H_6/O_2/N_2$ 3:6:91) with the total flow of 7 mL min^{-1} and 40 mg catalyst loading (diluted with SiC in order to avoid local overheating, as described in ref 64). (Mo,V)O_x was studied in the temperature regime between 260 and 290 °C, and catalytic tests for (Mo,V,Te,Nb)O_x were conducted in the temperature regime between 380 and 420 °C. For comparison, the conditions applied by Wernbacher et al. have been chosen.[8] The reaction products were finally detected by an Agilent 6890 gas chromatograph.

Propane Oxidation. The propane oxidation experiments were carried out in a single-tube fixed-bed reactor (quartz reactor, ID = 8 mm) with plug flow characteristics (instrument ID = E78) at atmospheric pressure and under steady state conditions. 88 mg of (Mo,V,Te,Nb)O_x and 100 mg of (Mo,V)O_x respectively, were loaded into the reactor. The catalyst bed was fixed in the isothermal zone of the reactor by two quartz wool plugs, and the catalysts were not diluted with an inert material. A total flow of 14.7 mL min^{-1} for (Mo,V,Te,Nb)O_x and 16.7 mL min^{-1} for (Mo,V)O_x, which was composed of 3% propane, 6% oxygen, 40% steam, and 51% helium, was used. The mass to flow ratio W/F (w8 hly space velocity (WHSV)) was 0.36 g s ml^{-1}. The gaseous reactant feed was mixed with mass flow controllers (EL-FLOW, Bronkhorst) using C_3H_8 (purity 3.5), C_3H_6 (purity 3.5), O_2 (purity 5.0), and N_2 (purity 5.0) (Westfalen AG). Steam was added to the gas flow through a vaporizer. The investigated temperature range was 250−300 °C for (Mo,V)O_x and 250−420 °C (Mo,V,Te,Nb)O_x. The product gas mixtures were analyzed by online gas chromatography (Agilent 7890 GC). The following GC column combinations were used for product analysis: (1) Plot-Q (30 m length, 0.53 mm internal diameter, 40 μm film thickness) plus Plot-MoleSieve 5 A (30 m length, 0.53 mm internal diameter, 50 μm film thickness), connected to a thermal conductivity detector (TCD) for analysis of the permanent gases (CO, CO_2, and O_2), and (2) Plot-Q (30 m length, 0.53 mm internal diameter, 40 μm film thickness) plus FFAP (30 m length, 0.53 mm internal diameter, 1 μm film thickness) connected to a flame ionization detector (FID) for analysis of hydrocarbons and oxygenates.

The conversion X_{Ri} in the catalytic reaction was calculated product-based:

$$X_R = \frac{\sum_j (\Delta C_{P_j})}{C_{R_0}} \quad (1)$$

https://doi.org/10.1021/acscatal.3c05230
ACS Catal. 2024, 14, 9018−9033

$$S_{P_j} = \frac{\Delta C_{P_j}}{\sum_j \Delta C_{P_j}} \tag{2}$$

where R_i and P_j are reactants and products, respectively; C_x is the amount of carbon in mol corresponding to the compound x; 0 corresponds to the reactants mixture; and Δ marks the difference between the mixture of products and reactants.

Laboratory Powder X-ray Diffraction (XRD). Laboratory powder X-ray diffraction (XRD) measurements were performed in Bragg−Brentano geometry on a Bruker AXS D8 Advance II θ/θ diffractometer using Ni filtered Cu $K\alpha_{1+2}$ radiation and a position-sensitive energy-dispersive LynxEye silicon strip detector. The sample powder was filled into the cavity of a silicon crystal low background sample holder, the surface of the powder bed being at the level of sample holder surface (front loading). The XRD patterns were recorded in continuous scanning mode in the range of 6−140° 2θ with an increment of 0.02° and a counting time of 1 s step^{-1}, resulting in a total accumulation time of 185 s per data point.

Whole powder pattern fitting according to the Rietveld method was performed with the TOPAS software (version 5, Bruker AXS, 1999−2014). For $(Mo,V)O_x$, the single crystal structure from the Supporting Information of Trunschke et al. was used.[40] Lattice parameters, peak profiles, and a pronounced preferred orientation were refined, while all atomic coordinates and occupation factors remained fixed. The fit with this rigid model already performed very well (Figure 1). Thus, a further refinement of the metal positions and occupancies was not done, since the reliability of such a refinement would be inferior compared to the original single crystal structure refinement. Concerning the $(Mo,V,Te,Nb)O_x$ data, the combined synchrotron/neutron powder refinement of DeSanto et al.[13] (ICSD-55097) was used as a starting model. Since the metal stoichiometry of our sample differed significantly from that of DeSanto et al., both the coordinates of the metal atoms and the occupations of partial (Te) and mixed (Mo/V) sites were refined in addition to the peak profiles and lattice parameters. The oxygen positions, however, were kept fixed at the published values to avoid overfitting. The resulting fit is shown in Figure 1.

Temperature-Dependent XRD. Temperature-dependent XRD measurements were performed on the quinary sample using a Bruker D-8 Discover system with Cu $K\alpha_1$ radiation from a primary Ge(111) Johannson monochromator and VANTEC position-sensitive detector in Bragg−Brentano mode. The sample was prepared on a substrate. A closed cycle helium cryostat (PheniX, Oxford Cryosystems) was used. Data were collected over a range of 2θ = 2−110°.

Rietveld refinements of the model determined above were performed using TOPAS v6.[65] The background was described using Chebychev polynomials of 22nd order, a one_on_x correction for increased air scattering at low angles, and two additional pseudo-Voigt peaks. The Lorentz-polarization factor was set to 27.3. Corrections for detector offset, specimen displacement, and surface roughness were refined for 300 K and then fixed for all other temperatures. The peak shape was described by a simple axial model, Gaussian and Lorentzian broadening due to crystallite size, and an orthorhombic Stephens model for strain at 300 K and also fixed for the other temperatures.[66]

Modeling the Stability of Various Surface Terminations by MLIP Calculations. The model selection is described in MLIP Surface Simulations. To judge which of the possible surface terminations is most likely observed in experiments, we then make use of *ab initio* thermodynamics[48] and calculate the surface free energy of the surface on (100) facet, $\gamma_{surf}^{(100)}$, as

$$\gamma_{surf}^{(100)} = \frac{1}{2A^{(100)}}\left[G_{surf}^{(100)} - \sum_i n_i\mu_i\right] \tag{3}$$

Here, $\gamma_{surf}^{(100)}$ is the surface free energy of the symmetrical surface slab model normalized to the surface area $A^{(100)}$, $G_{surf}^{(100)}$ is the Gibbs free energy of the surface slab calculated from GAP, and μ_i are the DFT-calculated chemical potentials of the various constituting species (i = Mo, V, Nb, O). The number of atoms of species i within the unit cell of the motif model is given by n_i.

Assuming that the motif is in thermodynamic equilibrium with the respective bulk M1 phase, we can define the Gibbs free energy of M1 bulk Mo_5O_{14} with the chemical potential of molybdenum (μ_{Mo}) and oxygen (μ_O) as $G_{Mo5O14} = 5\mu_{Mo} + 14\mu_O$. The chemical potential of oxygen μ_O is referenced to half the DFT total energy of the gas-phase oxygen molecule E_{O2} including zero-point energy (ZPE) contributions[67] and calculated as $\mu_O = \Delta\mu_O + \frac{1}{2}E_{O_2}$. Thus, the final working equation to determine the surface free energy of $(Mo,V)O_x$ surface slabs becomes

$$\begin{aligned}\gamma_{(Mo,V)O_x}^{(100)}(\Delta\mu_O) = \frac{1}{2A^{(100)}}\Bigg[&E_{(Mo,V)O_x,MLIP}^{(100)} - \frac{n_V^{(100)}}{10}\cdot E_{Mo_{30}V_{10}O_{112}} \\ &- \left(\frac{n_{Mo}^{(100)} - 3n_V^{(100)}}{40}\right)E_{Mo_{40}O_{112}} \\ &- \left(\frac{1}{2}E_{O_2,ZPE} + \Delta\mu_O\right)\left(n_O^{(100)} - (11.2n_V^{(100)}\right. \\ &\left. + 2.8(n_{Mo}^{(100)} - 3n_V^{(100)}))\right)\Bigg]\end{aligned} \tag{4}$$

Similarly, the surface free energy of Nb-containing $(Mo,V,Nb)O_x$ surface slabs is defined as

$$\begin{aligned}\gamma_{(Mo,V,Nb)O_x}^{(100)}(\Delta\mu_O) = \frac{1}{2A^{(100)}}\Bigg[&E_{(Mo,V,Nb)O_x,MLIP}^{(100)} - \frac{n_{Nb}^{(100)}}{4}\cdot E_{Mo_{26}Nb_4V_{10}O_{112}} \\ &- \left(\frac{n_V^{(100)} - 2.5n_{Nb}^{(100)}}{10}\right)\cdot E_{Mo_{30}V_{10}O_{112}} \\ &- \left(\frac{n_{Mo}^{(100)} - (3(n_V^{(100)} - 2.5n_{Nb}^{(100)}) + 6.5n_{Nb}^{(100)})}{40}\right)\Delta E_{Mo_{40}O_{112}} \\ &- \left(\frac{1}{2}E_{O_2,ZPE} + \Delta\mu_O\right)\left(n_O^{(100)} - (28n_{Nb}^{(100)} + 11.2(n_V^{(100)} - 2.5n_{Nb}^{(100)})\right. \\ &\left. + 2.8(n_{Mo}^{(100)} - (3(n_V^{(100)} - 2.5n_{Nb}^{(100)}) + 6.5n_{Nb}^{(100)}))))\Bigg]\end{aligned} \tag{5}$$

The relative chemical potential of oxygen $\Delta\mu_O = \Delta\mu_O(T, p)$ yields the dependence of the Gibbs free energy on temperature T and oxygen partial pressure p.[68] Assuming that the surrounding O_2 atmosphere behaves as an ideal-gas-like reservoir, μ_O is given by

$$\mu_O(T, p) = \mu_O(T, p^\circ) + \frac{1}{2}kT\ln\left(\frac{p}{p^\circ}\right) \tag{6}$$

https://doi.org/10.1021/acscatal.3c05230
ACS Catal. 2024, 14, 9018−9033

The temperature-dependent chemical potential of oxygen at the standard state pressure $\mu_O(T,p^\circ)$ is obtained from tabulated experimental data.[69] The experimental ZPE for O_2 molecule has been taken into account for its vibrational free energy contribution to the total energy.[67]

To calculate the training data set for MLIP, all density-functional theory (DFT) calculations are performed with first-principles semilocal DFT using the Perdew−Burke−Ernzerhof (PBE) exchange-correlation functional.[70] The periodic boundary condition calculations are computed using a planewave basis set together with SG15-optimized norm-conserving Vanderbilt pseudopotentials[71] taken from the PseudoDojo library[72] as implemented in Quantum ESPRESSO software package.[73] The kinetic cutoff energy for the expansion of the wave function and the charge density are set to 80 and 320 Ry, respectively. The Brillouin zone is integrated with a uniform reciprocal distance of 0.05 $Å^{-1}$, generating Γ-centered (1 × 1 × 6) k-point grids for bulk M1 and Mo_5O_{14}. To achieve a more accurate electronic structure of the M1 system, Hubbard *U*-corrected DFT has been applied to the Mo 4d, V 3d, and Nb 4d states using effective on-site parameters of 0.11, 0.45, and 0.61 eV, respectively. The values of *U* have been chosen according to the linear-response approach developed by Cococcioni and de Gioncoli.[74] Semiempirical van der Waals (vdW) correction due to Grimme with zero damping (PBE +D3) has been used for long-range dispersion correction.[75] Convergence criteria for the total energy and forces have been chosen as 10^{-6} and 10^{-5} Ry per atom, respectively. The lattice parameter optimization of the bulk M1 and Mo_5O_{14} has been followed by minimizing the stress tensor including all internal degrees of freedom until the external pressure reaches below 0.5 kbar. Geometry optimization for all surface calculations employed local Broyden−Fletcher−Goldfarb-Shanno (BFGS) minimization[76−78] until all force components and the total energy residual changes fell below 0.3 meV $Å^{-1}$ and 14 μeV, respectively.

For the bootstrapping, bulk materials and building block approach with motif structures taken from the previous study[23] and staged training scheme[47] have been used in the training protocol of MLIP for the efficient training. Gaussian approximation potential (GAP) was used for both ternary $(Mo,V)O_x$ and quaternary $(Mo,V,Nb)O_x$ systems.[79−81] For the quaternary $(Mo,V,Nb)O_x$ system, a compressing method for the SOAP descriptor was applied due to its memory requirement.[82,83] Detailed training methods are given in the Supporting Information.

PDF Data Acquisition, Treatment, and Refinement. For PDF analysis, XRD measurements were carried out at 65.4 keV (0.18957 Å) at Diamond Light Source at beamline I15-1 (XPDF) using a PerkinElmer detector XRD 4343 CT (432 × 432 mm^2 active area, 150 × 150 $μm^2$ pixel size). Each data set was collected for a total of 6 min; 12 data collections of 30 s each were performed and then averaged. All samples were measured in 1 mm Kapton capillaries using an empty capillary as background. A NIST ceria standard was used for distance calibration and instrumental resolution determination. The instrumental parameters are Q_{damp} = 0.0251 and Q_{broad} = 0.0124. Radial integration, masking, and normalization of the data were done at the beamline using automated processing in the DAWN software package.[84] PDF data were calculated with PDFgetX3[85] with Q_{min} = 0.43 $Å^{-1}$ and Q_{max} = 22.9 $Å^{-1}$ for $(Mo,V,Te,Nb)O_x$ and Q_{min} = 0.4 $Å^{-1}$ and Q_{max} = 22.4 $Å^{-1}$ for $(Mo,V)O_x$. For PDF calculations, the sample compositions have been used as determined by elemental analysis, *i.e.*, $Mo_{18.4}V_{7.9}O_{73.7}$ and $Mo_{18.3}V_{3.9}Nb_{2.9}Te_{2.0}O_{72.9}$.

PDF refinements were performed using TOPAS v6, taking advantage of the algorithm for fast simulation of PDFs from the structure model. The structure models as determined from the Rietveld refinements were used as the starting point. Refined parameters included the lattice parameters (*a, b, c*), a global scale factor, domain size damping according to log-normal spherical domain distribution (this was only used to get a slightly better fit to the damping profile, no further conclusions are drawn from the resulting parameter values), and B_{eq} values for each element, *i.e.*, B_{eq}(Mo), B_{eq}(V), and B_{eq}(O) for $MoVO_x$ and B_{eq}(Mo), B_{eq}(V), B_{eq}(Nb), B_{eq}(Te), and B_{eq}(O) for MoV_xNbTeO_x. The instrumental resolution parameters Q_{damp} and Q_{broad} (as defined in Diffpy-CMI) were fixed after determination by refinement to the CeO_2 standard. Refinements performed as a function of atomic site displacement bound were performed sequentially starting from low, *i.e.*, most highly constrained, bound windows. Refinements as a function of *r*-range were performed sequentially starting with high-*r* ranges, *i.e.*, more average-like structure, respectively.

Rules for Analyzing the Displacive Distortions. To allow flexibility in the refinement of the short-range structure while also constraining the model to avoid the occurrence of interatomic distances that are not physically meaningful, we have implemented rules to the fit model based on the following assumptions:

1. The atomic fractional coordinates were allowed to refine only in accordance with the crystal symmetry to keep the number of fit parameters low.
2. The coordinates of Mo and V on mixed -ccupancy metal sites have been constrained to the same value.
3. Disorder sites in the average structure, *i.e.*, described by split occupancy sites located at metal or channel sites, have been averaged back to a single site.
4. A constraint, D_r, *i.e.*, the maximum allowed displacement of the atoms, was set to limit the magnitude (in *x*, *y*, and *z* directions) of atomic site displacements from their average structure positions.

■ ASSOCIATED CONTENT

Supporting Information

The Supporting Information is available free of charge at https://pubs.acs.org/doi/10.1021/acscatal.3c05230.

XRD, SEM-EDX, catalytic test, original and additional images, the real structure of the bulk, further information on theoretical modeling and PDF analysis, additional structural models, and evaluation of the atomic displacement parameter (PDF)

■ AUTHOR INFORMATION

Corresponding Author

Thomas Lunkenbein − *Fritz-Haber-Institut der Max-Planck-Gesellschaft, 14195 Berlin, Germany;* orcid.org/0000-0002-8957-4216; Email: lunkenbein@fhi-berlin.mpg.de

Authors

Liudmyla Masliuk − *Fritz-Haber-Institut der Max-Planck-Gesellschaft, 14195 Berlin, Germany*

Kyeonghyeon Nam − *Fritz-Haber-Institut der Max-Planck-Gesellschaft, 14195 Berlin, Germany*

https://doi.org/10.1021/acscatal.3c05230
ACS Catal. 2024, 14, 9018−9033

Maxwell W. Terban − *Max Planck Institute for Solid State Research, 70569 Stuttgart, Germany;* orcid.org/0000-0002-7094-1266
Yonghyuk Lee − *Fritz-Haber-Institut der Max-Planck-Gesellschaft, 14195 Berlin, Germany;* orcid.org/0000-0001-8961-2254
Pierre Kube − *Fritz-Haber-Institut der Max-Planck-Gesellschaft, 14195 Berlin, Germany*
Daniel Delgado − *Fritz-Haber-Institut der Max-Planck-Gesellschaft, 14195 Berlin, Germany*
Frank Girgsdies − *Fritz-Haber-Institut der Max-Planck-Gesellschaft, 14195 Berlin, Germany*
Karsten Reuter − *Fritz-Haber-Institut der Max-Planck-Gesellschaft, 14195 Berlin, Germany;* orcid.org/0000-0001-8473-8659
Robert Schlögl − *Fritz-Haber-Institut der Max-Planck-Gesellschaft, 14195 Berlin, Germany; Department of Heterogeneous Reactions, Max Planck Institute of Chemical Energy Conversion, 45470 Mülheim a.d. Ruhr, Germany*
Annette Trunschke − *Fritz-Haber-Institut der Max-Planck-Gesellschaft, 14195 Berlin, Germany;* orcid.org/0000-0003-2869-0181
Christoph Scheurer − *Fritz-Haber-Institut der Max-Planck-Gesellschaft, 14195 Berlin, Germany*
Mirijam Zobel − *Institute of Crystallography, RWTH Aachen University, 52066 Aachen, Germany;* orcid.org/0000-0002-8207-8316

Complete contact information is available at: https://pubs.acs.org/10.1021/acscatal.3c05230

Author Contributions

[▽]Both authors contributed equally to the work.

Funding

Open access funded by Max Planck Society.

Notes

The authors declare no competing financial interest.

■ ACKNOWLEDGMENTS

Dr. Johannes Noack and Dr. Sabrina Jung are gratefully acknowledged for the synthesis of (Mo,V)O_x and (Mo,V,Te,Nb)O_x, respectively, during their stays at the FHI. Wiebke Frandsen and Gisela Weinberg are thanked for SEM and EDX analyses. We are further grateful of the XRF measurements conducted by Dr. Olaf Timpe. We acknowledge beamtime allocated at I15-1 (XPDF), Diamond Light Source, and thank Phil Chater for local support. Christine Stefani, Frank Adams, and Sebastian Bette are thanked for help with the temperature-dependent XRD measurements. L.M. thanks the Deutsche Forschungsgemeinschaft (DFG, German Research Foundation) (388390466 TRR 247) for funding. T.L. acknowledges support from the Federal Ministry of Education and Research in the framework of the project Catlab (03EW0015A). This work was further supported by to the Deutsche Forschungsgemeinschaft (DFG, German Research Foundation) under Germany's Excellence Strategy (EXC 2089/1-390776260).

■ REFERENCES

(1) Ren, T.; Patel, M.; Blok, K. Olefins from conventional and heavy feedstocks: Energy use in steam cracking and alternative processes. *Energy* **2006**, *31* (4), 425−451.
(2) Thorsteinson, E. M.; Wilson, T. P.; Young, F. G.; Kasai, P. H. The oxidative dehydrogenation of ethane over catalysts containing mixed oxides of molybdenum and vanadium. *J. Catal.* **1978**, *52* (1), 116−132.
(3) Gärtner, C. A.; van Veen, A. C.; Lercher, J. A. Oxidative Dehydrogenation of Ethane: Common Principles and Mechanistic Aspects. *ChemCatChem.* **2013**, *5* (11), 3196−3217.
(4) Chen, Y.; Yan, B.; Cheng, Y. State-of-the-Art Review of Oxidative Dehydrogenation of Ethane to Ethylene over MoVNbTeOx Catalysts. *Catalysts* **2023**, *13* (1), 204.
(5) Botella, P.; Dejoz, A.; Abello, M. C.; Vázquez, M. I.; Arrúa, L.; López Nieto, J. M. Selective oxidation of ethane: Developing an orthorhombic phase in Mo-V-X (X = Nb, Sb, Te) mixed oxides. *Catal. Today* **2009**, *142* (3−4), 272−277.
(6) Ishikawa, S.; Goto, Y.; Kawahara, Y.; Inukai, S.; Hiyoshi, N.; Dummer, N. F.; Murayama, T.; Yoshida, A.; Sadakane, M.; Ueda, W. Synthesis of Crystalline Microporous Mo-V-Bi Oxide for Selective (Amm)Oxidation of Light Alkanes. *Chem. Mater.* **2017**, *29* (7), 2939−2950.
(7) Ishikawa, S.; Kobayashi, D.; Konya, T.; Ohmura, S.; Murayama, T.; Yasuda, N.; Sadakane, M.; Ueda, W. Redox Treatment of Orthorhombic $Mo_{29}V_{11}O_{112}$ and Relationships between Crystal Structure, Microporosity and Catalytic Performance for Selective Oxidation of Ethane. *J. Phys. Chem. C* **2015**, *119* (13), 7195−7206.
(8) Wernbacher, A. M.; Kube, P.; Hävecker, M.; Schlögl, R.; Trunschke, A. Electronic and Dielectric Properties of MoV-Oxide (M1 Phase) under Alkane Oxidation Conditions. *J. Phys. Chem. C* **2019**, *123* (21), 13269−13282.
(9) Kube, P.; Frank, B.; Wrabetz, S.; Krohnert, J.; Havecker, M.; Velasco-Velez, J.; Noack, J.; Schlogl, R.; Trunschke, A. Functional Analysis of Catalysts for Lower Alkane Oxidation. *ChemCatChem.* **2017**, *9* (4), 573−585.
(10) Melzer, D.; Mestl, G.; Wanninger, K.; Zhu, Y.; Browning, N. D.; Sanchez-Sanchez, M.; Lercher, J. A. Design and synthesis of highly active MoVTeNb-oxides for ethane oxidative dehydrogenation. *Nat. Commun.* **2019**, *10*, 4012.
(11) Sanchez Sanchez, M.; Girgsdies, F.; Jastak, M.; Kube, P.; Schlögl, R.; Trunschke, A. Aiding the Self-Assembly of Supramolecular Polyoxometalates under Hydrothermal Conditions To Give Precursors of Complex Functional Oxides. *Angew. Chem., Int. Ed.* **2012**, *51* (29), 7194−7197.
(12) Nieto, J. M. L.; Botella, P.; Vázquez, M. I.; Dejoz, A. The selective oxidative dehydrogenation of ethane over hydrothermally synthesised MoVTeNb catalysts. *Chem. Commun.* **2002**, No. 17, 1906−1907.
(13) DeSanto, P.; Buttrey, D. J.; Grasselli, R. K.; Lugmair, C. G.; Volpe, A. F.; Toby, B. H.; Vogt, T. Structural aspects of the M1 and M2 phases in MoVNbTeO propane ammomidation catalysts. *Z. Kristallogr.* **2004**, *219* (3), 152−165.
(14) Murayama, H.; Vitry, D.; Ueda, W.; Fuchs, G.; Anne, M.; Dubois, J. L. Structure characterization of orthorhombic phase in MoVTeNbO catalyst by powder X-ray diffraction and XANES. *Applied Catalysis A: General* **2007**, *318* (0), 137−142.
(15) Sadakane, M.; Yamagata, K.; Kodato, K.; Endo, K.; Toriumi, K.; Ozawa, Y.; Ozeki, T.; Nagai, T.; Matsui, Y.; Sakaguchi, N.; Pyrz, W. D.; Buttrey, D. J.; Blom, D. A.; Vogt, T.; Ueda, W. Synthesis of Orthorhombic Mo-V-Sb Oxide Species by Assembly of Pentagonal Mo_6O_{21} Polyoxometalate Building Blocks. *Angew. Chem., Int. Ed.* **2009**, *48* (21), 3782−3786.
(16) Grasselli, R. Fundamental Principles of Selective Heterogeneous Oxidation Catalysis. *Top. Catal.* **2002**, *21* (1−3), 79−88.
(17) Vogt, T.; Blom, D. A.; Jones, L.; Buttrey, D. J. ADF-STEM Imaging of Nascent Phases and Extended Disorder Within the Mo-V-Nb-Te-O Catalyst System. *Top. Catal.* **2016**, *59*, 1489−1495.
(18) Blom, D. A.; Vogt, T.; Allard, L. F.; Buttrey, D. J. Observation of Sublattice Disordering of the Catalytic Sites in a Complex Mo-V-Nb-Te-O Oxidation Catalyst Using High Temperature STEM Imaging. *Top. Catal.* **2014**, *57* (14), 1138−1144.
(19) Pyrz, W. D.; Blom, D. A.; Sadakane, M.; Kodato, K.; Ueda, W.; Vogt, T.; Buttrey, D. J. Atomic-level imaging of Mo-V-O complex

oxide phase intergrowth, grain boundaries, and defects using HAADF-STEM. *Proc. Natl. Acad. Sci. U. S. A.* **2010**, *107* (14), 6152−6157.
(20) Pyrz, W. D.; Blom, D. A.; Sadakane, M.; Kodato, K.; Ueda, W.; Vogt, T.; Buttrey, D. J. Atomic-Scale Investigation of Two-Component MoVO Complex Oxide Catalysts Using Aberration-Corrected High-Angle Annular Dark-Field Imaging. *Chem. Mater.* **2010**, *22* (6), 2033−2040.
(21) Xu, P.; Sanchez-Sanchez, M.; Van Veen, A. C.; Browning, N. D.; Lercher, J. A. Ex-situ and in-situ analysis of MoVTeNb oxide by aberration-corrected scanning transmission electron microscopy. *Microscopy and Microanalysis* **2014**, *20* (3), 108−109.
(22) Lunkenbein, T.; Masliuk, L.; Plodinec, M.; Algara-Siller, G.; Jung, S.; Jastak, M.; Kube, P.; Trunschke, A.; Schlögl, R. Site specific and localized structural displacements in open structured multi-metallic oxides. *Nanoscale* **2020**, *12* (12), 6759−6766.
(23) Masliuk, L.; Heggen, M.; Noack, J.; Girgsdies, F.; Trunschke, A.; Hermann, K. E.; Willinger, M.-G.; Schloegl, R.; Lunkenbein, T. Structural Complexity in Heterogeneous Catalysis: Cataloging Local Nano-Structures. *J. Phys. Chem. C* **2017**, *121* (43), 24093−24103.
(24) Aouine, M.; Epicier, T.; Millet, J. M. M. In Situ Environmental STEM Study of the MoVTe Oxide M1 Phase Catalysts for Ethane Oxidative Dehydrogenation. *ACS Catal.* **2016**, *6* (7), 4775−4781.
(25) Zhu, Y.; Sushko, P. V.; Melzer, D.; Jensen, E.; Kovarik, L.; Ophus, C.; Sanchez-Sanchez, M.; Lercher, J. A.; Browning, N. D. Formation of Oxygen Radical Sites on MoVNbTeOx by Cooperative Electron Redistribution. *J. Am. Chem. Soc.* **2017**, *139* (36), 12342−12345.
(26) He, Q.; Woo, J.; Belianinov, A.; Guliants, V. V.; Borisevich, A. Y. Better Catalysts through Microscopy: Mesoscale M1/M2 Intergrowth in Molybdenum-Vanadium Based Complex Oxide Catalysts for Propane Ammoxidation. *ACS Nano* **2015**, *9* (4), 3470−3478.
(27) Pyrz, W. D.; Blom, D. A.; Vogt, T.; Buttrey, D. J. Direct imaging of the MoVTeNbO M1 phase using an aberration-corrected high-resolution scanning transmission electron microscope. *Angew. Chem., Int. Ed.* **2008**, *47* (15), 2788−2791.
(28) Melzer, D.; Xu, P.; Hartmann, D.; Zhu, Y.; Browning, N. D.; Sanchez-Sanchez, M.; Lercher, J. A. Atomic-Scale Determination of Active Facets on the MoVTeNb Oxide M1 Phase and Their Intrinsic Catalytic Activity for Ethane Oxidative Dehydrogenation. *Angew. Chem., Int. Ed.* **2016**, *55* (31), 8873−8877.
(29) Naumann d'Alnoncourt, R.; Csepei, L.-I.; Hävecker, M.; Girgsdies, F.; Schuster, M. E.; Schlögl, R.; Trunschke, A. The reaction network in propane oxidation over phase-pure MoVTeNb M1 oxide catalysts. *J. Catal.* **2014**, *311*, 369−385.
(30) Hävecker, M.; Wrabetz, S.; Kröhnert, J.; Csepei, L.-I.; Naumann d'Alnoncourt, R.; Kolen'ko, Y. V.; Girgsdies, F.; Schlögl, R.; Trunschke, A. Surface chemistry of phase-pure M1MoVTeNb oxide during operation in selective oxidation of propane to acrylic acid. *J. Catal.* **2012**, *285* (1), 48−60.
(31) Nguyen, T. T.; Deniau, B.; Baca, M.; Millet, J. M. M. Influence of Nb Content on the Structure, Cationic and Valence Distribution and Catalytic Properties of MoVTe(Sb)NbO M1 Phase Used as Catalysts for the Oxidation of Light Alkanes. *Top. Catal.* **2016**, *59* (17−18), 1496−1505.
(32) Valente, J. S.; Armendáriz-Herrera, H.; Quintana-Solórzano, R.; Del Ángel, P.; Nava, N.; Massó, A.; López Nieto, J. M. Chemical, structural, and morphological changes of a MoVTeNb catalyst during oxidative dehydrogenation of ethane. *ACS Catal.* **2014**, *4* (5), 1292−1301.
(33) Kasatkin, I.; Kurr, P.; Kniep, B.; Trunschke, A.; Schlögl, R. Role of Lattice Strain and Defects in Copper Particles on the Activity of Cu/ZnO/Al2O3 Catalysts for Methanol Synthesis. *Angew. Chem., Int. Ed.* **2007**, *46* (38), 7324−7327.
(34) Kardash, T. Y.; Lazareva, E. V.; Svintsitskiy, D. A.; Ishchenko, A. V.; Bondareva, V. M.; Neder, R. B. The evolution of the M1 local structure during preparation of VMoNbTeO catalysts for ethane oxidative dehydrogenation to ethylene. *RSC Adv.* **2018**, *8* (63), 35903−35916.
(35) Li, X.; Lunkenbein, T.; Pfeifer, V.; Jastak, M.; Nielsen, P. K.; Girgsdies, F.; Knop-Gericke, A.; Rosowski, F.; Schlögl, R.; Trunschke, A. Selective Alkane Oxidation by Manganese Oxide: Site Isolation of MnOx Chains at the Surface of MnWO4 Nanorods. *Angew. Chem., Int. Ed.* **2016**, *55* (12), 4092−4096.
(36) Li, X.; Teschner, D.; Streibel, V.; Lunkenbein, T.; Masliuk, L.; Fu, T.; Wang, Y.; Jones, T.; Seitz, F.; Girgsdies, F.; Rosowski, F.; Schlögl, R.; Trunschke, A. How to control selectivity in alkane oxidation? *Chemical Science* **2019**, *10* (8), 2429−2443.
(37) He, Q.; Woo, J.; Belianinov, A.; Guliants, V. V.; Borisevich, A. Y. Better Catalysts through Microscopy: Mesoscale M1/M2 Intergrowth in Molybdenum-Vanadium Based Complex Oxide Catalysts for Propane Ammoxidation. *ACS Nano* **2015**, *9* (4), 3470−3478.
(38) Grasselli, R. K.; Buttrey, D. J.; DeSanto, P.; Burrington, J. D.; Lugmair, C. G.; Volpe, A. F.; Weingand, T. Active centers in Mo-V-Nb-Te-Ox (amm)oxidation catalysts. *Catal. Today* **2004**, *91−92*, 251−258.
(39) Masliuk, L.; Schmidt, F.-P.; Hetaba, W.; Plodinec, M.; Auffermann, G.; Hermann, K.; Teschner, D.; Girgsdies, F.; Trunschke, A.; Schlögl, R.; Lunkenbein, T. Compositional Decoupling of Bulk and Surface in Open-Structured Complex Mixed Oxides. *J. Phys. Chem. C* **2020**, *124* (42), 23069−23077.
(40) Trunschke, A.; Noack, J.; Trojanov, S.; Girgsdies, F.; Lunkenbein, T.; Pfeifer, V.; Hävecker, M.; Kube, P.; Sprung, C.; Rosowski, F.; Schlögl, R. The Impact of the Bulk Structure on Surface Dynamics of Complex Mo-V-based Oxide Catalysts. *ACS Catal.* **2017**, *7* (4), 3061−3071.
(41) DeSanto, P.; Buttrey, D. J.; Grasselli, R. K.; Lugmair, C. G.; Volpe, A. F.; Toby, B. H.; Vogt, T. Structural characterization of the orthorhombic phase M1 in MoVNbTeO propane ammoxidation catalyst. *Top. Catal.* **2003**, *23* (1−4), 23−38.
(42) Arce-Ramos, J. M.; Rugg, G.; Genest, A.; Rösch, N. Probing the Positions of TeO Moieties in the Channels of the MoVNbTeO M1 Catalyst: A Density Functional Theory Model Study. *Catal. Lett.* **2021**, *151*, 2884−2893.
(43) Konya, T.; Katou, T.; Murayama, T.; Ishikawa, S.; Sadakane, M.; Buttrey, D.; Ueda, W. An orthorhombic Mo_3VO_x catalyst most active for oxidative dehydrogenation of ethane among related complex metal oxides. *Catal. Sci. Technol.* **2013**, *3* (2), 380−387.
(44) Trunschke, A.; Bellini, G.; Boniface, M.; Carey, S. J.; Dong, J.; Erdem, E.; Foppa, L.; Frandsen, W.; Geske, M.; Ghiringhelli, L. M.; Girgsdies, F.; Hanna, R.; Hashagen, M.; Hävecker, M.; Huff, G.; Knop-Gericke, A.; Koch, G.; Kraus, P.; Kröhnert, J.; Kube, P.; Lohr, S.; Lunkenbein, T.; Masliuk, L.; Naumann d'Alnoncourt, R.; Omojola, T.; Pratsch, C.; Richter, S.; Rohner, C.; Rosowski, F.; Rüther, F.; Scheffler, M.; Schlögl, R.; Tarasov, A.; Teschner, D.; Timpe, O.; Trunschke, P.; Wang, Y.; Wrabetz, S. Towards Experimental Handbooks in Catalysis. *Top. Catal.* **2020**, *63* (19), 1683−1699.
(45) Zhang, W.; Trunschke, A.; Schlögl, R.; Su, D. Real-Space Observation of Surface Termination of a Complex Metal Oxide Catalyst. *Angew. Chem., Int. Ed.* **2010**, *49* (35), 6084−6089.
(46) Wang, F.; Ueda, W. Preparation, characterization and catalytic performance of Mo-V-O oxide layers linked by alkylamines. *Chem. Commun.* **2009**, No. 9, 1079−1081.
(47) Lee, Y.; Timmermann, J.; Panosetti, C.; Scheurer, C.; Reuter, K. Staged Training of Machine-Learning Potentials from Small to Large Surface Unit Cells: Efficient Global Structure Determination of the RuO2(100)-c(2 × 2) Reconstruction and (410) Vicinal. *J. Phys. Chem. C* **2023**, *127* (35), 17599−17608.
(48) Reuter, K. Ab Initio Thermodynamics and First-Principles Microkinetics for Surface Catalysis. *Catal. Lett.* **2016**, *146* (3), 541−563.
(49) Billinge, S. J. L.; Kanatzidis, M. G. Beyond crystallography: the study of disorder, nanocrystallinity and crystallographically challenged materials with pair distribution functions. *Chem. Commun.* **2004**, No. 7, 749−760.
(50) Billinge, S. J.; Levin, I. The problem with determining atomic structure at the nanoscale. *Science* **2007**, *316* (5824), 561−5.

https://doi.org/10.1021/acscatal.3c05230
ACS Catal. 2024, 14, 9018−9033

(51) Ueda, W.; Vitry, D.; Kato, T.; Watanabe, N.; Endo, Y. Key aspects of crystalline Mo-V-O-based catalysts active in the selective oxidation of propane. *Res. Chem. Intermediat* **2006**, *32* (3−4), 217−233.
(52) Chupas, P. J.; Chapman, K. W.; Chen, H.; Grey, C. P. Application of high-energy X-rays and Pair-Distribution-Function analysis to nano-scale structural studies in catalysis. *Catal. Today* **2009**, *145* (3), 213−219.
(53) Schönauer, T.; Thomä, S. L. J.; Kaiser, L.; Zobel, M.; Kempe, R. General Synthesis of Secondary Alkylamines by Reductive Alkylation of Nitriles by Aldehydes and Ketones. *Chem.-Eur. J.* **2021**, *27* (5), 1609−1614.
(54) Newton, M. A.; Di Michiel, M.; Ferri, D.; Fernàndez-Garcia, M.; Beale, A. M.; Jacques, S. D. M.; Chupas, P. J.; Chapman, K. W. Catalytic Adventures in Space and Time Using High Energy X-rays. *Catalysis Surveys from Asia* **2014**, *18* (4), 134−148.
(55) Lunkenbein, T.; Girgsdies, F.; Wernbacher, A.; Noack, J.; Auffermann, G.; Yasuhara, A.; Klein-Hoffmann, A.; Ueda, W.; Eichelbaum, M.; Trunschke, A.; Schlögl, R.; Willinger, M. G. Direct Imaging of Octahedral Distortion in a Complex Molybdenum Vanadium Mixed Oxide. *Angew. Chem., Int. Ed.* **2015**, *54* (23), 6828−6831.
(56) Ok, K. M.; Halasyamani, P. S.; Casanova, D.; Llunell, M.; Alemany, P.; Alvarez, S. Distortions in Octahedrally Coordinated d0 Transition Metal Oxides: A Continuous Symmetry Measures Approach. *Chem. Mater.* **2006**, *18* (14), 3176−3183.
(57) Shannon, R. Revised effective ionic radii and systematic studies of interatomic distances in halides and chalcogenides. *Acta Crystallogr., Sect. A* **1976**, *32* (5), 751−767.
(58) Grasselli, R. K.; Burrington, J. D.; Buttrey, D. J.; DeSanto, P.; Lugmair, C. G.; Volpe, A. F.; Weingand, T. Multifunctionality of active centers in (amm)oxidation catalysts: from Bi-Mo-O-x to Mo-V-Nb-(Te, Sb)-O-x. *Top. Catal.* **2003**, *23* (1−4), 5−22.
(59) Heracleous, E.; Lemonidou, A. A. Ni-Nb-O mixed oxides as highly active and selective catalysts for ethene production via ethane oxidative dehydrogenation. Part I: Characterization and catalytic performance. *J. Catal.* **2006**, *237* (1), 162−174.
(60) Vendelbo, S. B.; Elkjær, C. F.; Falsig, H.; Puspitasari, I.; Dona, P.; Mele, L.; Morana, B.; Nelissen, B. J.; van Rijn, R.; Creemer, J. F.; Kooyman, P. J.; Helveg, S. Visualization of oscillatory behaviour of Pt nanoparticles catalysing CO oxidation. *Nat. Mater.* **2014**, *13* (9), 884−890.
(61) Dumesic, J. A.; Huber, G. W.; Boudart, M., Principles of Heterogeneous Catalysis. In *Handbook of Heterogeneous Catalysis*; Wiley-VCH, 2008.
(62) Ek, M.; Ramasse, Q. M.; Arnarson, L.; Georg Moses, P.; Helveg, S. Visualizing atomic-scale redox dynamics in vanadium oxide-based catalysts. *Nat. Commun.* **2017**, *8*, 305.
(63) Schlögl, R. Heterogeneous catalysis. *Angew. Chem., Int. Ed.* **2015**, *54* (11), 3465−3520.
(64) Cotter, T. P. The reducibility of mixed Mo/V oxide materials to carbides and their reactivity in the activation of propane. Ph.D. Thesis, Technische Universität Berlin, Berlin, Germany, 2011.
(65) Coelho, A. TOPAS and TOPAS-Academic: an optimization program integrating computer algebra and crystallographic objects written in C++. *J. Appl. Crystallogr.* **2018**, *51* (1), 210−218.
(66) Stephens, P. Phenomenological model of anisotropic peak broadening in powder diffraction. *J. Appl. Crystallogr.* **1999**, *32* (2), 281−289.
(67) Irikura, K. K. Experimental Vibrational Zero-Point Energies: Diatomic Molecules. *J. Phys. Chem. Ref. Data* **2007**, *36* (2), 389−397.
(68) Reuter, K.; Scheffler, M. Composition, structure, and stability of RuO_2 (110) as a function of oxygen pressure. *Phys. Rev. B* **2001**, *65* (3), 035406.
(69) Chase, M. *NIST-JANAF Thermochemical Tables*, 4th ed.. American Institute of Physics, 1998.
(70) Perdew, J. P.; Burke, K.; Ernzerhof, M. Generalized Gradient Approximation Made Simple. *Phys. Rev. Lett.* **1996**, *77* (18), 3865−3868.
(71) Hamann, D. R. Optimized norm-conserving Vanderbilt pseudopotentials. *Phys. Rev. B* **2013**, *88* (8), 085117.
(72) van Setten, M. J.; Giantomassi, M.; Bousquet, E.; Verstraete, M. J.; Hamann, D. R.; Gonze, X.; Rignanese, G. M. The PseudoDojo: Training and grading a 85 element optimized norm-conserving pseudopotential table. *Comput. Phys. Commun.* **2018**, *226*, 39−54.
(73) Giannozzi, P.; Andreussi, O.; Brumme, T.; Bunau, O.; Buongiorno Nardelli, M.; Calandra, M.; Car, R.; Cavazzoni, C.; Ceresoli, D.; Cococcioni, M.; Colonna, N.; Carnimeo, I.; Dal Corso, A.; de Gironcoli, S.; Delugas, P.; DiStasio, R. A.; Ferretti, A.; Floris, A.; Fratesi, G.; Fugallo, G.; Gebauer, R.; Gerstmann, U.; Giustino, F.; Gorni, T.; Jia, J.; Kawamura, M.; Ko, H. Y.; Kokalj, A.; Küçükbenli, E.; Lazzeri, M.; Marsili, M.; Marzari, N.; Mauri, F.; Nguyen, N. L.; Nguyen, H. V.; Otero-de-la-Roza, A.; Paulatto, L.; Poncé, S.; Rocca, D.; Sabatini, R.; Santra, B.; Schlipf, M.; Seitsonen, A. P.; Smogunov, A.; Timrov, I.; Thonhauser, T.; Umari, P.; Vast, N.; Wu, X.; Baroni, S. Advanced capabilities for materials modelling with Quantum ESPRESSO. *J. Phys.: Condens. Matter* **2017**, *29* (46), 465901.
(74) Cococcioni, M.; de Gironcoli, S. Linear response approach to the calculation of the effective interaction parameters in the *LDA+U* method. *Phys. Rev. B* **2005**, *71* (3), 035105.
(75) Grimme, S.; Antony, J.; Ehrlich, S.; Krieg, H. A consistent and accurate ab initio parametrization of density functional dispersion correction (DFT-D) for the 94 elements H-Pu. *J. Chem. Phys.* **2010**, *132* (15), 154104.
(76) BROYDEN, C. G. The Convergence of a Class of Double-rank Minimization Algorithms 1. General Considerations. *IMA Journal of Applied Mathematics* **1970**, *6* (1), 76−90.
(77) Goldfarb, D. A family of variable-metric methods derived by variational means. *Mathematics of Computation* **1970**, *24*, 23−26.
(78) Shanno, D. F. Conditioning of Quasi-Newton Methods for Function Minimization. *Mathematics of Computation* **1970**, *24*, 647−656.
(79) Bartók, A. P.; Payne, M. C.; Kondor, R.; Csányi, G. Gaussian Approximation Potentials: The Accuracy of Quantum Mechanics, without the Electrons. *Phys. Rev. Lett.* **2010**, *104* (13), 136403.
(80) Deringer, V. L.; Bartók, A. P.; Bernstein, N.; Wilkins, D. M.; Ceriotti, M.; Csányi, G. Gaussian Process Regression for Materials and Molecules. *Chem. Rev.* **2021**, *121* (16), 10073−10141.
(81) Deringer, V. L.; Caro, M. A.; Csányi, G. Machine Learning Interatomic Potentials as Emerging Tools for Materials Science. *Adv. Mater.* **2019**, *31* (46), 1902765.
(82) Darby, J. P.; Kermode, J. R.; Csányi, G. Compressing local atomic neighbourhood descriptors. *npj Computational Materials* **2022**, *8*, 166.
(83) Bartók, A. P.; Kondor, R.; Csányi, G. On representing chemical environments. *Phys. Rev. B* **2013**, *87* (18), 184115.
(84) Filik, J.; Ashton, A. W.; Chang, P. C. Y.; Chater, P. A.; Day, S. J.; Drakopoulos, M.; Gerring, M. W.; Hart, M. L.; Magdysyuk, O. V.; Michalik, S.; Smith, A.; Tang, C. C.; Terrill, N. J.; Wharmby, M. T.; Wilhelm, H. Processing two-dimensional X-ray diffraction and small-angle scattering data in DAWN 2. *J. Appl. Crystallogr.* **2017**, *50* (3), 959−966.
(85) Juhas, P.; Davis, T.; Farrow, C. L.; Billinge, S. J. L. PDFgetX3: a rapid and highly automatable program for processing powder diffraction data into total scattering pair distribution functions. *J. Appl. Crystallogr.* **2013**, *46* (2), 560−566.

https://doi.org/10.1021/acscatal.3c05230
ACS Catal. 2024, 14, 9018−9033